SANDIA REPORT

10 MW$_e$ Solar Thermal Central Receiver Pilot Plant Receiver Performance Final Report

A. F. Baker

SF2900Q(8-81)

10 MW$_e$ SOLAR THERMAL CENTRAL RECEIVER PILOT PLANT RECEIVER PERFORMANCE FINAL REPORT

Alvin F. Baker
Project Engineering Division III
Sandia National Laboratories Livermore

ABSTRACT

This report uses experimental data to evaluate the performance of the 10 MW$_e$ Solar Thermal Central Receiver Pilot Plant receiver. Receiver performance includes such receiver characteristics as point-in-time steady state efficiency, average efficiency, receiver life, start-up time, operations time, and operations during cloud transients. The receiver peak steady state efficiency, calculated by two different methods, before December 1985 was about 77%. After the receiver was repainted in December 1985, the peak steady state efficiency increased to about 82%, near design predictions. The receiver average efficiency, although lower than the peak by 5 to 10 percentage points, shows a similar increase after the repainting. Receiver thermal losses (radiation, convection, and conduction), calculated by two different methods, are about 4.5–5.5 MW$_t$. Receiver life – which includes the effect of receiver start-up, operation time, operation during cloud transients, and panel supports – is an area requiring further evaluation. Within two years from the start of receiver operation, panel tube leaks began to occur. Receiver panel deformations, which continue to occur, will have an adverse effect on the receiver life.

FOREWORD

The research described in this report was conducted within the U. S. Department of Energy's Solar Thermal Technology Program. This program directs efforts to incorporate technically proven and economically competitive solar thermal options into our nation's energy supply. These efforts are carried out through a network of national laboratories that work with industry.

In a solar thermal system, mirrors or lenses focus sunlight onto a receiver where a working fluid absorbs the solar energy as heat. The system then converts the energy into electricity or uses it as process heat. There are two kinds of solar thermal systems: central receiver systems and distributed receiver systems. A central receiver system uses a field of heliostats (two-axis tracking mirrors) to focus the sun's radiant energy onto a receiver mounted on a tower. A distributed receiver system uses three types of optical arrangements – parabolic troughs, parabolic dishes, and hemispherical bowls – to focus sunlight onto either a line or point receiver. Distributed receivers may either stand alone or be grouped.

This report uses experimental data to evaluate the performance of the 10 MW_e Solar Thermal Central Receiver Pilot Plant receiver. This receiver, which has been in operation since February 1982, has provided the solar central receiver program with the first opportunity to evaluate receiver performance over a five-year period. After evaluating the receiver efficiency, start-up time, and operation time, improvements were implemented which increased the receiver efficiency, reduced start-up times, and increased operation time. After finding receiver panel tube leaks which reduce receiver life, modifications were made to the panels and operation procedures to eliminate certain types of tube leaks. Comparisons between experimental results and design predictions showed agreement for steady state efficiency, but the actual receiver life is expected to be well below the design life.

4.

CONTENTS

ILLUSTRATIONS

6

8

TABLES

Summary

This report uses experimental data to evaluate the performance of the 10 MW_e Solar Thermal Central Receiver Pilot Plant (Solar One) receiver. Our receiver performance evaluation included such receiver characteristics as point-in-time steady state efficiency, average efficiency, receiver life, start-up time, operation time, and operations during cloud transients. The Solar One pilot plant, shown in Figure 1, is located near Barstow, California and began operation in February 1982.
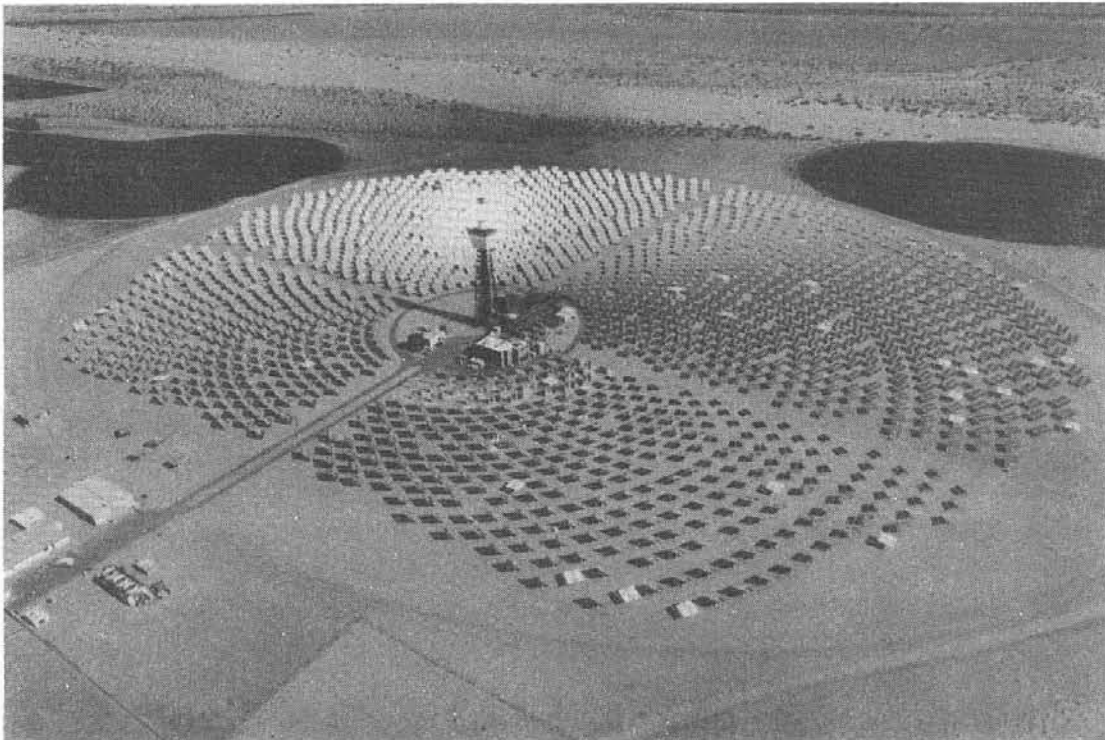
Figure 1. 10 MW_e Solar Thermal Central Receiver Pilot Plant (Solar One) in operation near Barstow, California.

The receiver at Solar One sets on top of a 64 m steel tower near the center of a surround heliostat field. Shown in Figure 1 as a bright glow, the receiver is just above the white trapezoidal targets near the top of the tower. At the base of the tower, inside the inner ring of heliostats in Figure 1, are the thermal storage subsystem, turbine/generator, and plant control building. Outside of the heliostat field in Figure 1 are administration and office buildings.

The receiver at Solar One is a 360° external type consisting of twenty-four 70 tube panels. Six of the panels are water preheat and eighteen are water-to-steam

11

boiler panels. The maximum peak solar flux density on the north boiler panels is 0.3 MW_t/m^2 and this flux density reduces to 0.1 MW_t/m^2 on the south water preheat panels.

We evaluated each receiver performance characteristic using measured data from summary data tapes of receiver operations. These data tapes covered the time period from December 1982 to December 1986. In addition to the data tapes, we used photographs of test specimen and receiver panels, results from analyses, and laboratory tests to evaluate some performance characteristics. We discussed problems and solutions and compared our results using different evaluation techniques to design prediction.

We found that our results for the peak receiver point-in-time efficiency, before the receiver was repainted in December 1985, was 76.7% ± 4%, nearly the same as earlier reported in References 4 and 5. This receiver efficiency and those reported in References 4 and 5 used a statistical method of least squares evaluation of steady state data for the receiver absorbed and incident powers. We used a different method to calculate the receiver point-in-time efficiency, independent of the receiver incident power. We found that this different method, thermal loss tests, gave a receiver efficiency of 76.1% ± 2.6% at a slightly lower value of the receiver absorbed power than the peak from the statistical method. We compared the results from both methods of calculating the receiver efficiency with the design predictions in Figure 2.

The two results using experimental data, data fit line and thermal loss test in Figure 2, gave nearly the same efficiency at the same value of the receiver absorbed power. However, both experimental results were lower than the design prediction, shown as "X's" in Figure 2. We found the difference between the experimental results and predictions could be accounted for, in part, by the difference in the value of the receiver surface solar absorptance. Measurements showed the receiver solar absorptance was less than 0.88 before December 1985 while predictions assumed a value of 0.95.

After repainting the receiver in December 1985, the measured receiver solar absorptance increased to 0.97, a value near that used for design predictions. We used the thermal loss test method to experimentally determine the receiver steady state efficiency after repainting the receiver. We found the receiver steady state efficiency, after repainting the receiver, increased to about 82%. This value is near the design values shown in Figure 2.

Our evaluation of the receiver average efficiency and operation time showed that these receiver characteristics increased each year of operation as we gained experience in receiver operation. Before the receiver was repainted, the receiver average efficiency was about 10 percentage points below the peak steady state efficiency. After repainting, the difference between the average and peak efficiency decreased to about 5 percentage points.
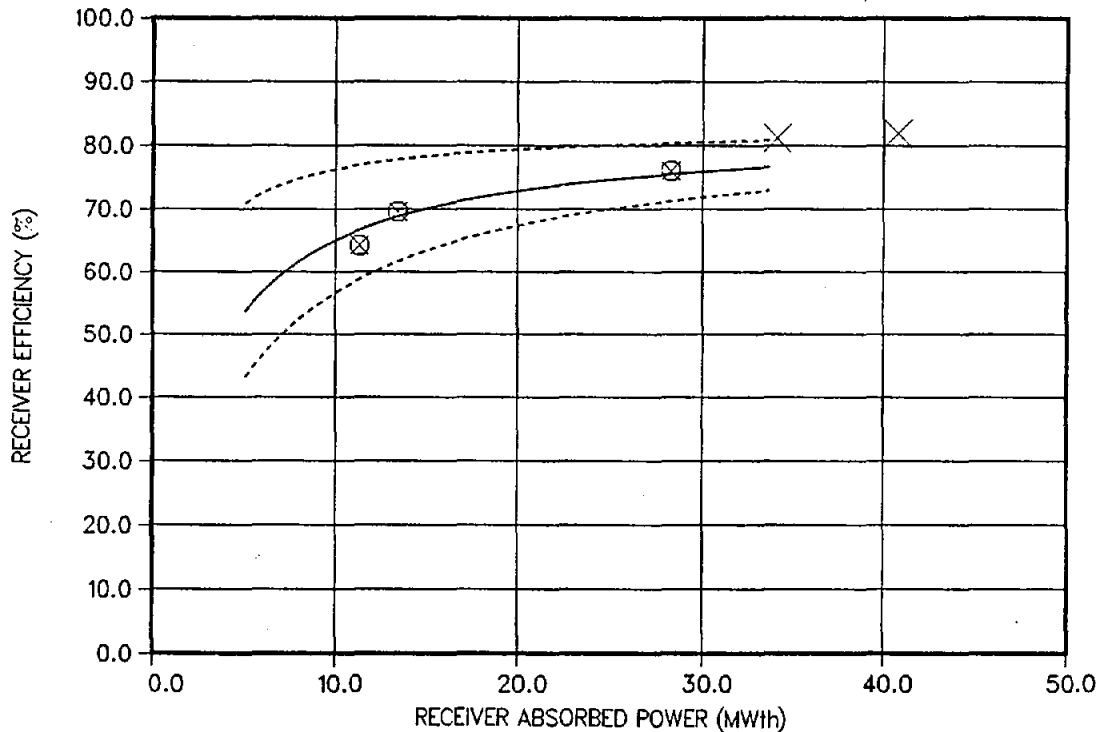
Figure 2. Receiver efficiency data fit line (solid line) and prediction interval
(dash lines) from the statistical method compared to the efficiencies
from the thermal loss test ($\otimes$) on October 31, 1985. The two "X's" are
design values from Reference 10.

The improvement in receiver average efficiency and operation time, before re-
painting, reflects experience in reducing receiver start-up time and an increasing
receiver operating time. After repainting the receiver, we implemented improve-
ments in the receiver start-up heliostat field aimpoints, which decreased start-up
times even more than before repainting. The increased receiver solar absorptance,
after repainting the receiver, also helped reduce start-up time and increase opera-
tion time.

We performed receiver thermal loss tests to further understand the receiver
performance and verify the results of the statistical method of least squares analysis
evaluation. The agreement between the receiver steady state efficiency using the
statistical method and loss tests was shown in Figure 2. We found the distribu-
tion of the frequency of occurrence of the receiver thermal loss using the statis-
tical method had the general shape of a normal distribution. The mean value
is 4.74 MW_t with an estimated standard deviation of 1.2 MW_t. The thermal
losses from the thermal loss tests ranged from a low of 4.36 MW_t to a high of
5.56 MW_t. These experimental results and the design predictions were all of the
same order of magnitude.

We used a qualitative approach to evaluate receiver operation during cloud
transients. We examined data plots of receiver operation on cloudy days and

13

compared these to the operation on a clear day. We found the receiver could continue to operate through large and continuous changes in the insolation if there is some time delay between these changes. However, associated with these changes in insolation, the receiver tube metal temperature experienced rapid changes. These temperature changes could affect the receiver life by low cycle fatigue and high thermal stresses.

The continuous operation of the Solar One receiver, since early February 1982, has provided an opportunity to evaluate receiver life. We found that after 18 months of operation, boiler panel tube leaks occurred near a weld at the top of the boiler panels. After 19 months, we found leaks on boiler panel north edge tubes at the top 90° bend. We made modifications at the top of the boiler panels and changed the operation procedures to eliminate these types of tube leaks. Also, we observed that the receiver boiler panels were showing signs of panel warping (radial deflection in and out along the panel normal) and bowing (decrease panel radius of curvature in the lateral or receiver circumferential direction). The six receiver water preheat panels showed no signs of panel deformations or tube leaks.

After 42 months of receiver operation, we found panel tube leaks on the back of the boiler panels where clips are welded to the panels to attach panel supports. These clip weld leaks first occurred on the upper portion of the panels, in the steam superheat section. We believe that the clip weld leaks are caused, among other factors, by thermal stresses in the weld region due to the temperature gradient between panel tube/clip weld and the clip material away from the tube. These clip weld leaks continue to occur, and as long as we have these types of clips welded to the panel, there is a chance we will have clip weld leaks. These clip weld leaks are repaired through the use of a grind and weld fill method.

Like the panel clip weld leaks, the panel warping and bowing is continuing on the boiler panels. The severity of the boiler panel deformation, shown in Figure 3 - a recent photograph of the top portion of several boiler panels, has increased with time. This panel warpage and bowing does not limit receiver operation; however, such deformations must be reducing the receiver life.

We believe this panel deformation is caused by the lateral temperature gradient across the panel and the temperature gradient from the front to the back of the panel. These temperature gradients are most severe in the upper portion of the panels, superheated steam region, where the heat transfer between the tube wall and steam is less than the subcooled water and boiling regions. Without a major re-design and modification to the receiver panel supports, we will not be able to eliminate all the problems affecting receiver life.

We have shown that our methodology for predicting receiver point-in-time efficiency and thermal losses gave reasonable results when compared to experimental data. However, improvement should be made in both the experimental

14
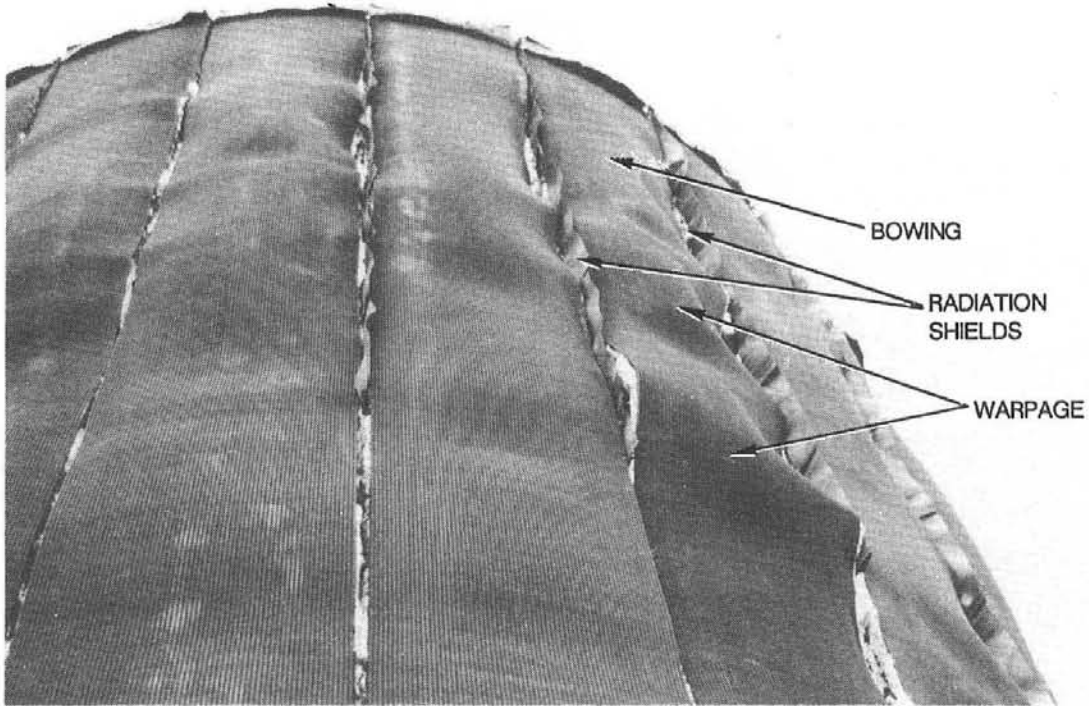
Figure 3. Photograph of the top portion of the receivers, showing the current panel warpage and bowing. The radiation shields installed between the panels protect the sides of the edge tubes from incident radiation.

and analytical techniques of evaluating these parameters. We believe it is unlikely that the Solar One receiver will have a 30-year life. Because receiver life is affected by receiver start-up, cloud transients, receiver shut down, and panel supports, this is an area which requires further evaluation.

10 MW$_e$ SOLAR THERMAL CENTRAL RECEIVER PILOT PLANT RECEIVER PERFORMANCE FINAL REPORT

Introduction

This report uses experimental data to evaluate the performance of the Solar One receiver. Receiver performance, shown pictorially in Figure 4, includes such receiver characteristics as point-in-time steady state efficiency, average efficiency, receiver life, start-up time, operation time, and operations during cloud transients. Each of these characteristics and related items will be covered in some detail in this report. Initial receiver performance, during the preoperation phase, was reported in Reference 4 and updated, during the early part of the test and evaluation phase, in Reference 5.
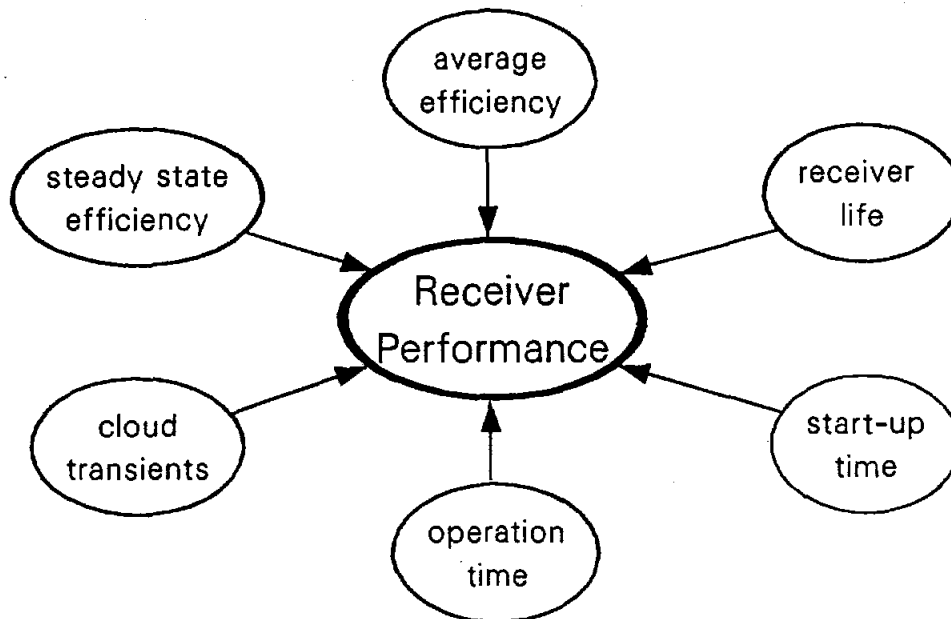
Figure 4. Receiver Performance Includes Several Receiver Characteristics Which are Related.

The sun's energy, reflected from the heliostat field, was first incident on the receiver at the 10 MW$_e$ Solar Thermal Central Receiver Pilot Plant (Solar One) located near Barstow, California, on February 3, 1982. This marked the beginning of the operation of the world's largest Solar Thermal Central Receiver Plant. The pilot plant continued to operate for over five years. Thus, Solar One is the only central receiver plant to provide long-term receiver performance data including receiver life.

The first operation phase was to check out the plant capabilities, develop operating procedures, and demonstrate the integrated operation of the plant control system. This preoperation phase at Solar One lasted for six months, until July 31, 1982, and the results are reported in Reference 1. Following the preoperation phase, the plant began a two-year test and evaluation phase. Its primary objectives were to characterize the operation and performance of all of the plant systems, for example, the heliostat field, receiver, thermal energy storage, and turbine generator. Finally, after completing the test and evaluation phase, the plant was operated in a utility environment for three years during a power production phase until July 31, 1987. References 2 and 3 provide an overview of the results from the test and evaluation and power production phases, respectively. Even though the official five-year program for Solar One ended on July 31, 1987, the plant continues to operate in a utility environment.

The primary source of experimental data for this evaluation is from "Summary Data Tapes". These tapes are developed from the data tapes produced by the Solar One Data Acquisition System (DAS). The data tapes contain data for:

direct normal insolation,

heliostats tracking the receiver,

wind speed and direction,

ambient air temperature,

receiver flow,

receiver inlet and outlet temperatures,

receiver metal temperatures,

receiver inlet and outlet pressures,

electric power production.

The DAS recorded data at sub-second intervals during the test and evaluation phase and at several second intervals during the power production phase. These DAS data tapes were processed and data at three minute intervals were written

to the summary data tapes. The summary data tapes for this report cover the time period from December 1982 through December 1986. Summary data tapes for year 1987 will be developed but were not available for this report. The summary data tapes do not contain all of the data during plant operations. During the four years covered, there were times when DAS was not operable, not started, or shut off early. The total hours of operation or total energies in this report may be different from those reported by others based on another source of data. These Solar One summary data tapes are available from Sandia National Laboratories, Albuquerque, N.M.

Whenever possible, results from the evaluation of Solar One experimental data are compared to predictions made by the plant designers. If differences exist, we attempt to understand those differences. The report first describes the receiver and the methods used to evaluate the data. Next, the performance results are reported and then compared to results from a different evaluation method. Finally, a narrative approach is used to discuss operation during cloud transients and receiver life. Finally, the report discusses problems concerning the operation and performance of the Solar One receiver and their solutions.

Receiver Description

This section provides a brief description of the Solar One receiver; more detail can be found in Reference 6. The receiver at Solar One is a cylindrical external receiver located near the middle of a surround heliostat field. The receiver surface consists of twenty-four panels, six water preheat panels and eighteen boiler panels. The boiler panels are once through water-to-steam; preheated water enters the bottom of each panel and exits as superheated steam. Unlike the other type of central receivers - cavity receivers - in which the heat absorbing surfaces are inside an exterior enclosure, the external receiver has its heat absorbing surface exposed to the environment.

Receiver Characteristics

The Solar One receiver is a right circular cylinder with a diameter of 7.01 m and total height of 13.72 m. The active heat absorbing height of the receiver is only 13.46 m since insulation covers a small portion of the top and bottom of the receiver surface. The surface of the cylinder is made up from twenty-four heat absorbing panel modules. The receiver is mounted vertically on top of a 64.31 m steel tower; the centerline of the receiver height is 78.64 m above the ground. Figure 5 is a photograph of the supporting tower and the receiver in operation. Figure 6 is a drawing of the receiver mounted on the tower. The receiver in Figure 5 appears to glow white like a giant light bulb, not because of its high operating temperature but because of reflected sun light from its surface. At the base of the tower in Figure 5 are the thermal storage system and the turbine/plant control

building. The thermal storage tank is the large tank behind the tower, and the thermal storage heat exchangers are to the right of the tower. The turbine/plant control building is to the right of the tower and forward of the thermal storage heat exchangers. The dark tank in the foreground is a water make-up tank.

In Figures 5 and 6 just below the receiver are four Beam Characterization System (BCS) targets which are used to look at individual heliostat beams. Data from the BCS are used for adjustment of the heliostat beams to reduce their pointing error. Instrumentation rooms located behind the BCS targets are shown in Figure 6. About halfway up the tower in Figure 6, wind sensor booms (one on the east and one on the west) have been installed to provide wind speed and direction data. Figure 6 shows the overall dimensions of the tower and receiver. An elevator for access to the receiver is located on the left side of the tower, and stairs are in the center of the tower.

The design peak incident solar flux density on the Solar One receiver is 0.3 MW_t/m^2 (300 times the intensity of the sun) and has a general trapezoidal distribution along the length of the panels. This peak flux density only occurs on the north most receiver panels and decreases to about 0.1 MW_t/m^2 on the south panels. Peak solar flux densities on the intermediate panels varies between these two values. The average solar flux density on the receiver at full power is about 0.16 MW_t/m^2.

The receiver panels are once through water-to-steam; thus subcooled water enters the bottom of the boiler panels and is heated by the solar flux. When the water reaches its boiling temperature, it goes through a phase change, liquid to steam, without an increase in temperature. Finally, the steam is superheated to the desired outlet temperature. Figure 7 shows a prediction of the front surface temperature (solid line) and solar flux density (dash line) distribution for a representative Solar One boiler panel. We see in Figure 7 (solid line); starting at the inlet (0 m), there is an increase in panel temperature, then a region of constant temperature, boiling, and an abrupt change in temperature at the start of the steam region, departure from nucleate boiling, with a further increase in temperature to superheat the steam. The slight decrease in the temperature at the top of the panel corresponds to the decrease in the solar flux density at the top.

The solar flux density distribution in Figure 7 (dash line) has a general trapezoidal shape with three "humps". These humps occur where there are three rings of heliostat field aimpoints on the surface of the receiver. More information about the heliostat field aimpoints can be found in References 4 and 15. The flux is zero at the panel bottom, increases to its peak and is high along the length of the panel, and decreases to zero at the panel top. This solar flux density distribution is the same for all receiver panels except the magnitude of the high portion decreases from the north to the south side of the receiver.

The Solar One receiver was designed to provide flexibility regarding the outlet steam temperature and pressure conditions. These conditions are determined

20

THERMAL STORAGE
TANK

HEAT
EXCHANGERS

CONTROL BUILDING

Figure 5. Photograph of the Solar One receiver in operation on the top of a the steel tower. At the base of the tower are the thermal storage tank, heat exchangers, and control building.
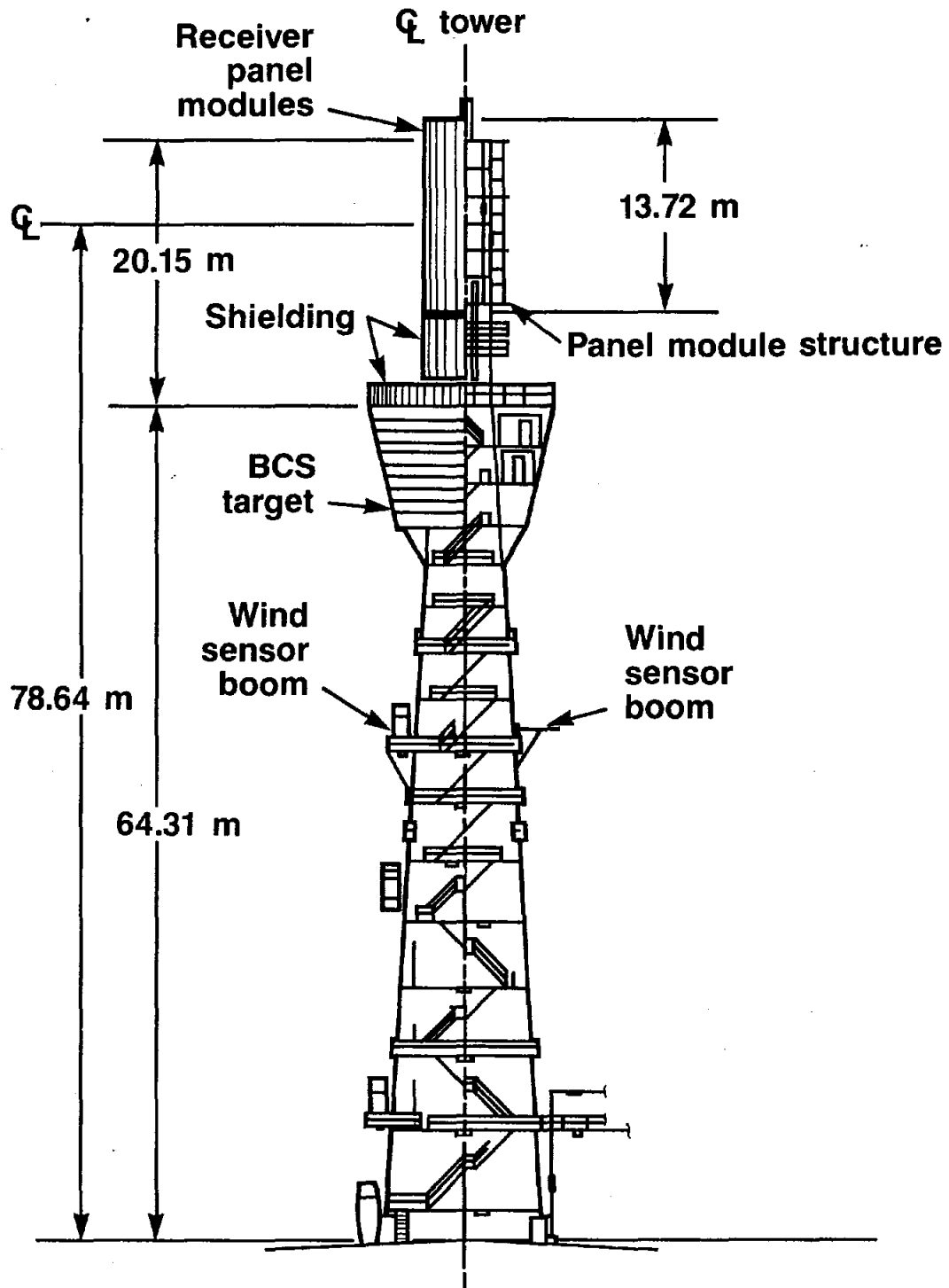
Figure 6. Drawing of the Solar One receiver on the top of the tower showing physical dimensions and equipment locations.
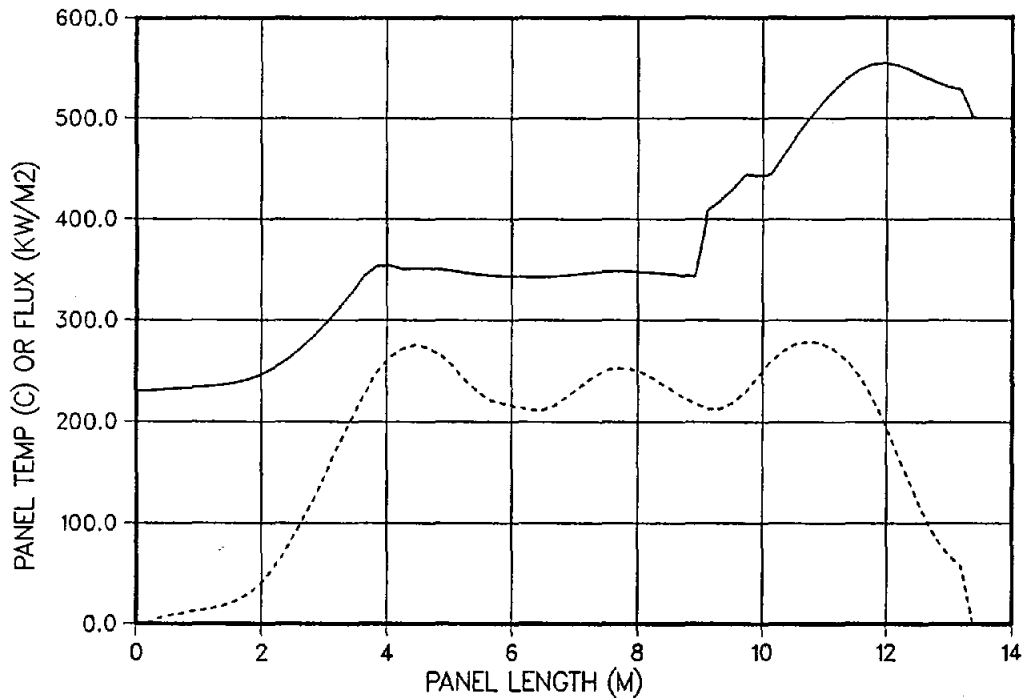
Figure 7. Prediction of the front surface temperature (solid line) and solar flux density (dash line) distribution for a representative Solar One boiler panel.

by how the receiver steam is used. Nominal steam conditions appropriate for turbine start-up, normal turbine operations, and thermal storage charging are listed below.

	Temperature (°C)	Pressure (MPa)
Turbine Start-up	415	5.5
Turbine Operation	415-510	5.5-10
Thermal Storage Charging	340-510	9-10

The only limitation to these flexible receiver outlet steam conditions is the total receiver flow. For example, the maximum flow limit to the turbine is 54,000 kg/hr and to thermal storage is 59,000 kg/hr. Also, during receiver start-up, before the receiver outlet steam has reached a superheated condition, the flow passes through the receiver flash tank. This flash tank is limited to 18,000 kg/hr flow and a pressure of 4.0 MPa. In general these flow limitations have not affected receiver operation at Solar One.

Table I summarizes the major characteristics of the Solar One receiver.

TABLE I

SOLAR ONE RECEIVER CHARACTERISTICS

Receiver configuration	360° external cylinder
Receiver diameter (m)	7.01
Receiver active height (m)	13.46
Receiver active area (m^2)	296.4
Receiver weight (kg)	150,000
Maximum absorbed power (MW$_t$)	37.00
Peak incident solar flux (MW$_t$/m^2)	0.30
Average solar flux (MW$_t$/m^2)	0.16

Panel Characteristics

The receiver surface consists of twenty-four heat absorbing panel modules. Each panel module consists of seventy tubes welded together along their lengths on the back surface. The exposed surface of each panel is coated with Pyromark (Reference 7), a high temperature, nonselective black paint. Tubes of each panel are welded into an inlet and outlet manifold, all made from Incoloy 800. Panel tubes have an outside diameter of 12.70 mm and a wall thickness of 2.93 mm. Each panel total width is 889 mm. Panel design features are covered in more detail in the Receiver Life section of this report and in Reference 6. Of the twenty-four panels, there are six water preheat panels and eighteen boiler panels. Preheat panels are located on the south side of the receiver. The receiver is a once-through water-to-steam receiver; subcooled water enters the receiver boiler panels and exits as superheated steam.

Figure 8, a photograph of the receiver not in operation, and Figure 9, a drawing, shows the receiver and gives the numbering scheme for the individual panels. The insulation, covering a small portion of the top and bottom of each receiver panel, is shown in Figure 8. Also, a small gap (about 50 mm) between each panel is visible in Figure 8. This small gap between the panels reduces the total receiver absorber area about 3.8% from the total active exposed area.

Figure 9 shows the overall dimensions of the receiver and the numbering scheme of the individual panels. Flow in all twenty-four panels is always upward from the bottom to the top. Panels 1, 2, 3, 22, 23, and 24 are water preheat panels—all of the water flow to the receiver flows first in three parallel paths through panels 1, 2, and 3 and then through panels 22, 23, and 24. The preheat panels are located on the south side of the receiver. These preheat panels raise the inlet water temperature several hundred degrees without allowing the water to boil. Panels 4
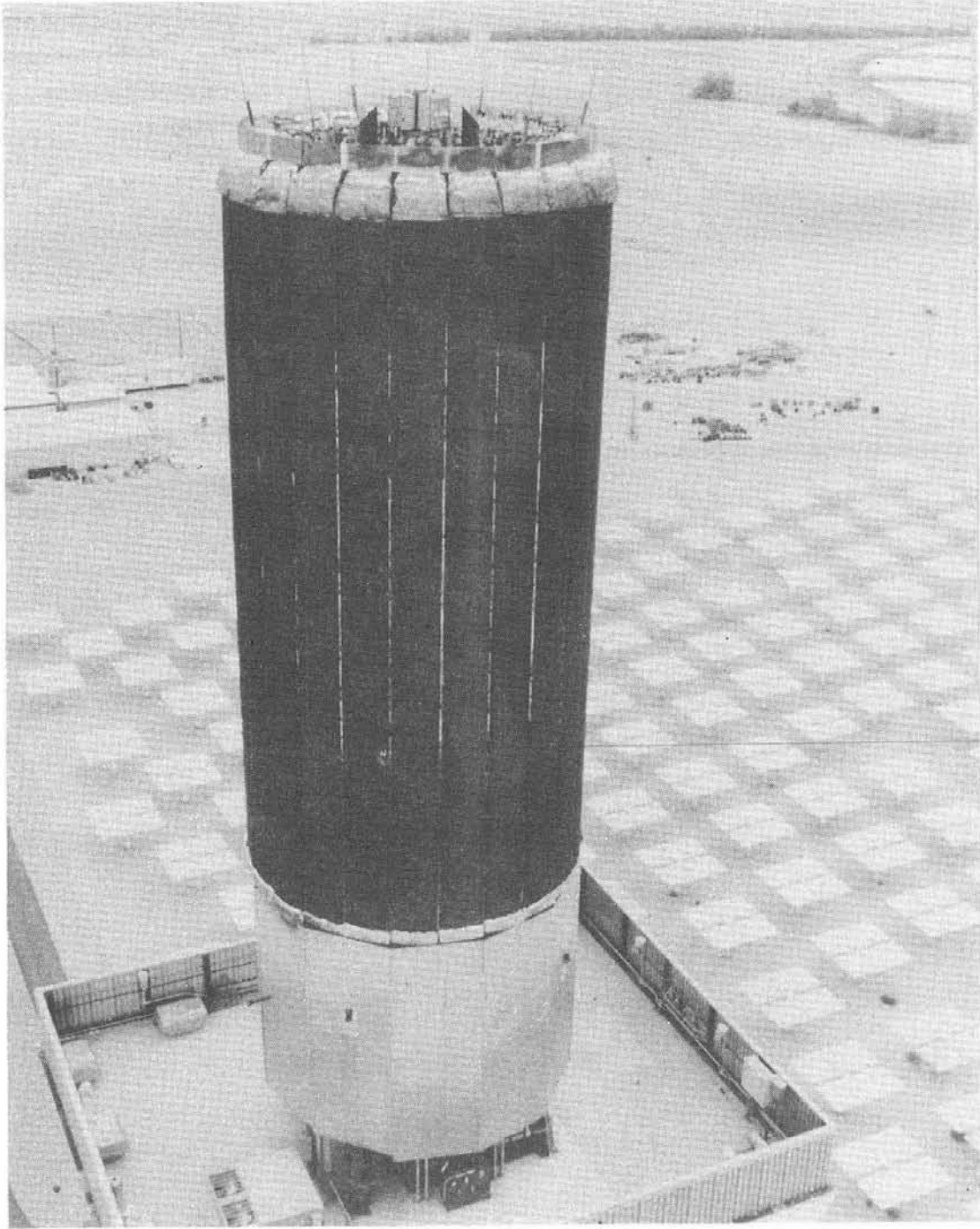
Figure 8. Photograph of the receiver (not operating) at the 10 MW$_e$ Solar Thermal Central Receiver Pilot Plant, Solar One, near Barstow, CA.

25

(Top view)

N

Panel orientation
and numbering
scheme

23ft
(7m)

Panel

44.7ft
(13.6m)

45ft
(13.7m)

Preheat (1-3) + (22-24)
Boiler/superheater 4-21
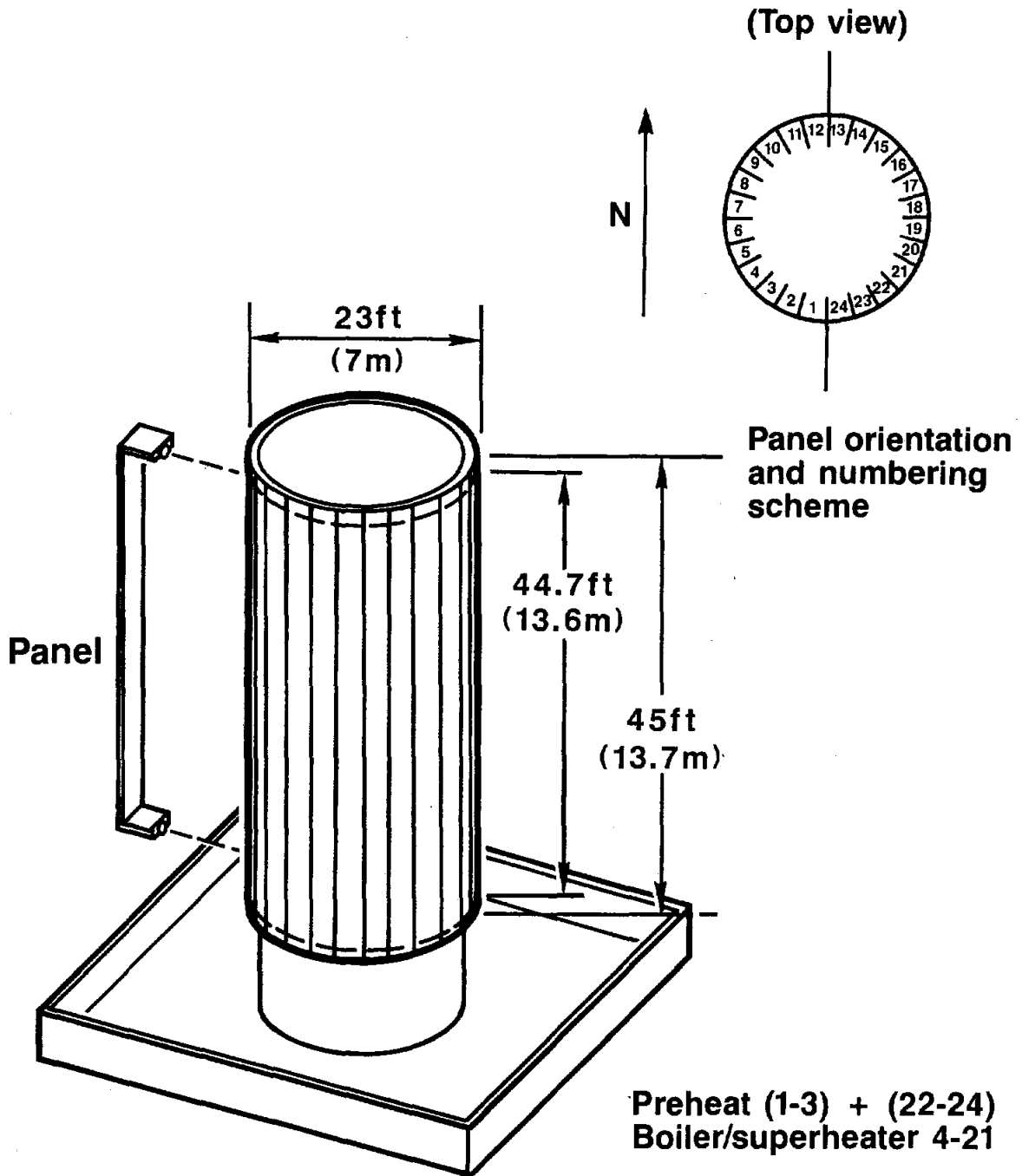
Figure 9. Drawing of the Solar One receiver showing overall physical dimensions
and panel numbers.

through 21 are boiler panels–the water from the six preheat panels flows in eighteen parallel paths and exits each boiler panel as superheated steam. To achieve the desired panel outlet temperature, each boiler panel has its own flow control valve and a flowmeter. These are located between a ring manifold supplying water to all of the boiler panels and the panel inlet manifold.

Table II summarizes the major characteristics of the Solar One receiver panels.

TABLE II

SOLAR ONE PANEL CHARACTERISTICS

Number of panels	6 water preheat
	18 boiler
Panel width (mm)	889
Panel active length (m)	13.46
Tubes per panel	70
Tube outside diameter (mm)	12.70
Tube wall thickness (mm)	2.93
Tube material	Incoloy 800

To achieve the desired flow and dynamic stability of the water/steam through the individual boiler panel tubes, orifices are installed at the inlets of the tubes. These orifices increase the single phase (water) pressure drop component of the total pressure loss through the tube. The panel edge tubes do not have inlet orifices. Depending on a panel's location on the receiver, the size of the orifices varies. The northernmost panels, 10 through 15, have the same single size orifices. East and west panels have graduated size orifices, depending on the panel location. The orifice sizes within a panel are used to adjust tube-to-tube flow rates according to the incident solar flux distribution across the width of a panel. Mirror image east and west panels have the same graduated size orifices. For example, panels 4 and 21 have similar orifices as do panels 5 and 20. However, the large orifices are on the right or north side of panel 21 as compared to those on panel 4 where the large orifices are on the left or north side. Most of the heliostats reflecting the sun's energy toward the receiver are located north of the receiver. The preheat panels have no orifices.

Instrumentation

The receiver description would not be complete without identifying some of the instrumentation on the individual panels. Data from part of the panel instrumentation was used in the receiver performance evaluation. Each panel has three flux gages which are exposed to the incident solar power reflected from the heliostat field. These flux gages are located at three elevations along the height of the

27

panels and are centered in the lateral direction next to tube 35. The purpose of these gages is to sense flux changes for receiver control.

All boiler panels, i.e, panels 4 through 21, have at least seven thermocouples mounted on the back surface (not exposed to the incident power from the heliostat field). Three of these thermocouples are for control purposes and are located at a panel elevation from the bottom of the panel at 11.71 m on tube 35 (center of the panel). The other four or five thermocouples are located at an elevation of 13.28 m on tubes 1, 5, 35, and 65 and on tube 70 if the panel is on the west side of the receiver. Panels 6, 12, 17, and 21 have even more thermocouples located on their back surface than the seven or eight already noted. These additional thermocouples are located at various panel elevations. Tubes 1 and 70 are panel edge tubes, while the others are interior tubes. In general the panel edge tubes are exposed to more incident solar radiation than the interior tubes since they are not protected on one side by an adjacent tube. North panel edge tubes tend to operate at higher temperatures than the interior tubes.

Each preheat panel has a thermocouple to measure outlet water temperatures. The ring manifold that connects to each of the boiler panels has temperature and pressure instrumentation. Boiler panels 4, 5, 8, 10, 12, 14, 17, 19, and 21 have thermocouples to measure inlet water temperature, and all boiler panels have three thermocouples to measure their outlet steam temperature; however, only one is recorded on DAS. Both the riser and downcomer, which connect to the receiver, have temperature and pressure instrumentation. Data from the ring manifold, panels, and receiver inlet and outlet instrumentation are used in the evaluation to calculate the panel and receiver absorbed power. More instrumentation exists, but since it is not used extensively for the receiver evaluation, it will not be described.

Evaluation Method

The measured data used to evaluate the Solar One receiver performance comes from the summary data tapes for the time period from December 1982 through December 1986. These data tapes contain point-in-time data recorded at three-minute intervals. In addition to the data tapes, measured data for the heliostat field reflectivity as a function of the day of the year was provided by the staff at Solar One. The data tapes contained site environmental data and receiver parameters for calculating the receiver absorbed power. The heliostat field performance was based on calculations using the MIRVAL heliostat field performance code developed by Sandia, Reference 8. The reflected solar power incident on the receiver, receiver incident power, used a "field performance value" and measured data including site insolation, mirror reflectivity, and actual number of heliostats tracking the receiver. The field performance value is an output from the MIRVAL code for the measured Solar One heliostat characteristics and field layout. By running MIRVAL for different sun positions, sun elevation and azimuthal angles, we can create a matrix of field performance values. This matrix is used to find the heliostat field performance value for any sun position–time of day–when the receiver incident power is calculated.

When we processed the data acquisition system tapes to create the summary data tapes, we flagged measurement gages which were either out of range or bad. When we used the summary data tapes, these flagged measurements were set to zero.

We utilized several techniques to select the actual value of a parameter from the summary data tape to be used in the performance evaluation. If there were two values of a parameter available, we calculated the average of the two measurements. We then checked to see if one of the values was within 5.0% of the average. When this value was within 5.0% of the average, the average value was used for this parameter. If the value was not within 5.0% of the average, the highest value of the two parameters was used if no other checks were possible.

There were no redundant pressure measurements on the data tapes, but there were pressure measurements at the receiver inlet, ring manifold, outlet, and base of the tower. A check was made to see that each down-stream pressure was less than the one before. If a pressure was less than the next down-stream value, we used the down stream value. We assumed that at least one of the pressure measurements was correct. Since enthalpy, used to calculate absorbed power, is not a strong function of pressure, a reasonable value for the pressure is adequate.

The ring manifold which feeds water to the eighteen boiler panels has a water temperature measurement as do nine of the boiler panel inlets. These nine inlet temperatures were sorted, low to high, and the fifth value was selected as a

redundant measurement to the ring manifold measurement. The technique used when there were two values for a parameter was applied to select the boiler panels inlet temperature to be used in the performance evaluation. This temperature was also used to correct the flow measurement for each boiler panel since the flowmeters were calibrated for a fixed temperature different from the actual operating conditions.

The total receiver flow and flow through each boiler panel were recorded on the data tapes. We added the flow through the boiler panels and used this sum as a redundant measurement to the total receiver flow. The technique used when there were two values for a parameter was applied to select the total receiver flow to be used in the performance evaluation. Once this value was selected, the individual panel flows were adjusted proportionally so that their sum was the same as the selected total receiver flow.

Receiver outlet temperature and individual boiler panel outlet temperatures were on the data tapes. Using the panel outlet temperatures and adjusted panel flows, we calculated a weighted average of the panels' outlet temperature. This temperature was assumed to be a redundant temperature to the receiver outlet temperature measurement. Again, the technique for two measurements was applied to find the receiver outlet temperature used for receiver performance.

There are three values of direct normal insolation on the summary data tapes from two separate measurement instruments. Two of these values are from the same instrument but processed by different instrumentation systems. To select the insolation used for the performance evaluation, we made several checks using the data. The first check was to insure that none of the values were above 50 w/m^2 before sunrise. If a measurement was above this value before sunrise, then that measurement was omitted for that day. After this check, each measurement value was considered redundant to the others, and the technique for two measurements of the same parameter was applied. As soon as a value within the 5.0% criteria was found, the process was terminated, and we used that average value. If none of the values met the 5.0% criteria, the highest value was selected for the performance evaluation.

To select the site wind speed from four values on the data tapes, the data were sorted, low to high. The lowest and highest values were omitted, and the average of the two remaining values was selected.

The receiver point-in-time efficiency used steady state conditions for the receiver absorbed and incident power. Efficiency is defined as:

$$Receiver\ efficiency = \frac{absorbed\ power}{incident\ power} \tag{1}$$

The receiver absorbed power is calculated from measured temperatures, pressures, and flow. In contrast, the incident power is calculated using measured insolation,

number of heliostats tracking the receiver, and mirror reflectivity and a predicted heliostat performance value.

To determine a steady state condition, data for several parameters over a thirty-three minute time interval (eleven consecutive data values from the summary data tapes) were fit with straight lines using a least squares technique. We compared each measured data value to the fitted value at the same instance in time. If the difference between the measured and fitted value was less than a specified amount, then a steady state condition was assumed to exist. For example, eleven consecutive values for the receiver outlet temperature were calculated from the data tape. These eleven values were fit with a straight line, and we calculated the average of the eleven values. If at each time step the difference between the measured value and fitted value was less than 1.0% of the calculated average temperature, we considered the outlet temperature to be at steady state. We used the value from the data fit equation at the tenth time interval as the steady state outlet temperature value. Parameters evaluated for steady state during the same thirty-three minute time interval were the insolation, number of heliostats tracking the receiver, receiver inlet and outlet temperatures and pressure, and receiver mass flow. Also, this same procedure for finding steady state was done for the calculated receiver incident and absorbed powers. All of these parameters had to satisfy the steady state criteria before we assumed the receiver to be at steady state. Receiver flow and inlet water temperature used 3.0% of the average value during the thirty-three minutes, the power values used 2.0% of the average, and all other parameters used 1.0% of the average for the steady state criteria.

When a steady state condition was found, then the next eleven consecutive data tape values were processed as before. If a steady state condition was not found, then all the data was incremented by one data tape time step and were processed as before. These steady state values were written to a file to be used in the point-in-time evaluation.

As indicated above the Solar One data tapes were processed for steady state conditions. These steady state data were written to a file along with relevant receiver and weather parameters. We searched this steady state file with selected parameters having a specified range of value; i.e., outlet temperature, number of heliostats tracking the receiver, and wind speed, and found data for the receiver absorbed and incident power for similar operating conditions. We then evaluated this data for similar operating conditions, using the method of least squares. In general we found that, within certain limits, the relationship of the incident power to the absorbed power did not change as the range in the parameters was changed. Typical ranges used for the receiver inlet temperature were 115 - 190°C, outlet temperature 415 - 460°C, heliostats tracking the receiver greater than 1000, and insolation above 500 w/m². Although smaller ranges in the parameters were investigated, the number of data points, when using a narrow range, did not cover a board range in receiver power levels. The data tended to be concentrated in a narrow range of operating power levels.

The evaluation of the relationship between the receiver absorbed power and incident power with the point-in-time steady state data was done using the statistics method of least squares, Reference 9. We assumed that there is a functional relationship between the receiver incident and absorbed power. We further assumed that the values of the receiver absorbed power which are calculated from measured data – measured temperatures, pressures, and flow – are more accurate than the receiver incident power. As mentioned earlier, the receiver incident power is calculated based on measured insolation, heliostats tracking the receiver, and mirror reflectivity and a predicted heliostat field performance value. Thus, the receiver absorbed power is considered the independent variable, more exact, and the receiver incident power the dependent variable, less predictable, for the evaluation.

The method of least squares evaluation of the steady state data allows us to determine a linear fit of the data and prediction interval estimates for the incident power given the receiver absorbed power. The linear fit of the receiver incident and absorbed power data provides an "expected value" of the receiver incident power, given a value of the absorbed power. For this study we calculated the 95% prediction interval for future values of the incident power corresponding to a given value of the absorbed power. Thus, based on the data between December 1982 and December 1986, given a future value of the receiver absorbed power, within the range used for the evaluation, the expected value of the incident power would lie on the linear fit line and there is a 95% probability that the incident power will be within the prediction interval. This prediction interval accounts for random errors in the receiver absorbed and incident powers calculated from the measured data. Bias errors, measurement instruments which always read either high or low, could shift the results either high or low, but the trend in the results would remain the same. Given the linear fit of the receiver absorbed and incident powers and prediction interval, we used these results to calculate the receiver efficiency as a function of the receiver absorbed power and its prediction interval. Unless otherwise indicated, the receiver efficiency is defined by Equation (1). Similar evaluations were performed to show the relationship of the receiver efficiency as a function of the site wind speed.

We used a two-step procedure to calculate a least squares fit of the data and the 95% prediction interval. The first step was to use all of the data from the steady state file within the limits of the selected parameters. This data was fit using the method of least squares, and an estimate of the variability about the fit line of the incident power was calculated. Using these results the original data was edited by eliminating those data sets where the incident power was more than twice the estimated variability from the fit line. The second step was to use the edited data and calculate a new linear fit of the data and 95% prediction interval. This process accounted for less than 10% of the original data being deleted.

Receiver average efficiency was determined by calculating the receiver absorbed and incident power at each instance of time on the data tapes. Receiver

absorbed power was calculated when the receiver delivered superheated steam to the bottom of the tower. This definition for the receiver absorbed power was selected since it is only when superheated steam is delivered to the bottom of the tower that this energy can be used to drive the steam turbine/generator or charge thermal energy storage. Receiver incident power was calculated when ever there were heliostats tracking the receiver. Thus, there is a time interval difference between the receiver absorbed and incident powers. Again, the receiver incident power was calculated using the MIRVAL field performance values. The receiver absorbed and incident powers were integrated over time for each day to calculate the daily average receiver performance. The daily energies were summed to find the receiver average performance values for some number of days. We define the average receiver efficiency as

$$Average\ receiver\ efficiency = \frac{average\ absorbed\ energy}{average\ incident\ energy} \qquad (2)$$

We performed receiver thermal loss tests to further understand the receiver performance and verify the results of the statistical method of evaluation. These receiver thermal loss test results were used to evaluate the receiver thermal loss and part load performance. In this report thermal loss includes receiver losses from emitted radiation, convection, and conduction while reflected radiation is accounted for by an effective receiver solar absorptance. Once we determined the receiver thermal loss from these loss tests, we calculated the receiver efficiency independent of knowing the receiver incident power. This receiver efficiency, found independent of the receiver incident power, was compared to the results from the statistical method which used the receiver incident power, Equation (1).

For each of the loss tests the receiver was operated at three different power levels by selecting the number and location within the heliostat field of which heliostats were tracking the receiver. The receiver inlet and outlet temperatures were near their normal operating conditions during the test. The heliostats selected to track the receiver were distributed throughout the heliostat field so the distribution of the incident power on the receiver was the same for each power level but the magnitude changed as a function of the number of heliostats tracking the receiver. The selection of which heliostats tracked the receiver is the key to the evaluation of the receiver performance for these tests. Appendix A shows the development of the equations used for the evaluation of these receiver thermal loss tests.

One of the three power levels used all available heliostats tracking the receiver, full power. *The other two power levels are less than full power, and we used complementary numbers of heliostats to track the receiver.* Thus, the sum of the heliostats tracking the receiver for the two reduced power levels is the same as that for the full power level – all available heliostats. The tests at the three different power levels are done on the same day, and we assumed that the heliostat field reflectivity was constant during that day. The tests are performed near solar

noon using one of the reduced power levels before noon, full power at noon, and the other reduced power after noon. The receiver is kept at each power level long enough for a steady state condition to be reached before changing to the next power level. By being near solar noon, the heliostat field performance value is nearly constant during the test. This test procedure allowed us to calculate the receiver thermal loss, efficiency, and part load efficiency, as a fraction of the full power efficiency, without knowing the receiver incident power while the receiver is operating at near normal conditions.

Performance Results

Receiver performance will be discussed in this and the next three sections of the report. This section is divided into three subsections covering point-in-time efficiency, average efficiency and operation time, and receiver start-up. To evaluate the receiver point-in-time steady state efficiency, we used data from the steady state file created from processing the summary data tapes. Average efficiency and operation time are from integration of the data on the summary data tapes. Receiver start-up is from the summary data tapes.

Point-In-Time Efficiency

The most often referred to receiver efficiency is a point-in-time efficiency at some reference point. The reference point is usually a particular day of the year and a time during that day with a specified value for the insolation. For the Solar One receiver the reference point is considered to be equinox noon with an insolation of 973 w/m^2. It is important to know how this point-in-time efficiency changes with time and insolation, that is, the value of its part load efficiency. A receiver which has a high peak efficiency and low part load efficiency may not produce as much annual energy as one which has a lower peak efficiency but good part load efficiency. Experience at Solar One has shown it is only on the clear days that the insolation exceeds 950 w/m^2, so the receiver seldom operates at its design reference point conditions.

To find the receiver steady state point-in-time efficiency, defined by Equation (1), we had to find steady state values for these two parameters. The steady state file was searched for receiver conditions where the wind speed was less than 6.7 mps (15 mph), inlet temperature between 115°C and 190°C, outlet temperature between 415°C and 460°C, and outlet pressure between 9.0 MPa and 10.3 MPa. There were 948 steady state data sets of receiver absorbed and incident power which met these conditions. We evaluated this data using the statistical method to find a linear fit of the data, 95% prediction interval, and variability of the data from the data fit line. The data was again evaluated after those data sets were deleted which had the receiver incident power more than twice the variability from the fit line. The final data set contained 898 data pairs which is 94.7% of the original data.

Using the evaluation method of least squares analysis, Figure 10 shows the receiver incident and absorbed power steady state data points (dots), linear fit of the data (solid line), and the 95% prediction interval for future observations of the incident power corresponding to a value of the absorbed power (dashed lines). The two "X's" shown in Figure 10 are September 1982 (Revised December 1985) design values before the plant began operation from Reference 10. These design values were based on a receiver outlet temperature of 515°C and a receiver solar absorptance of 0.95 for the Pyromark paint.
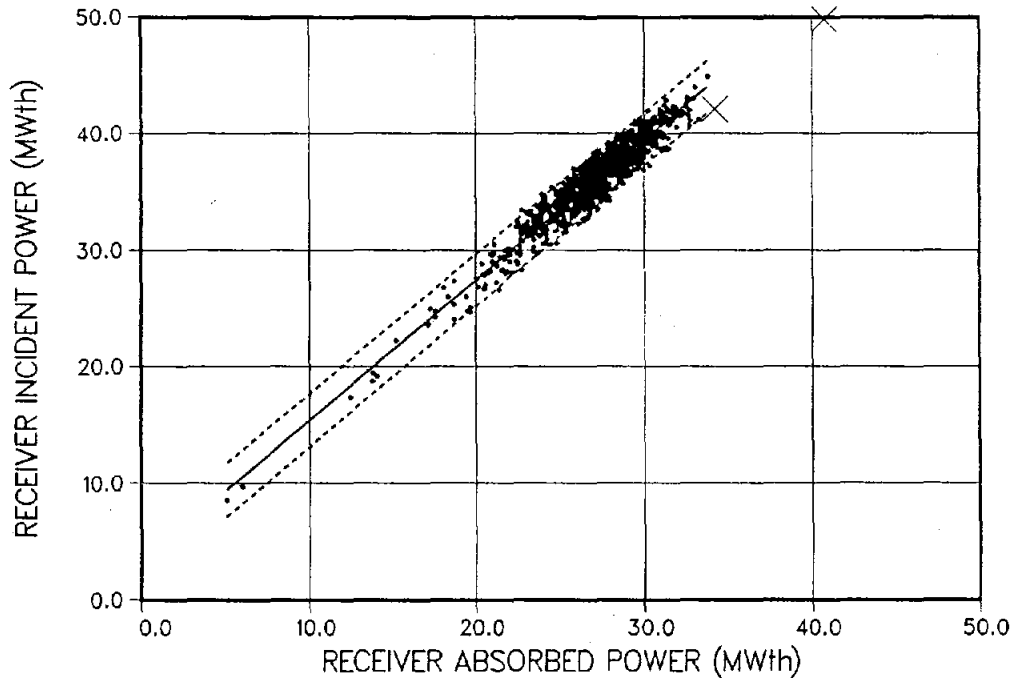
Figure 10. Calculated receiver incident power versus calculated absorbed power
data (dots), data fit (solid line), and 95% prediction interval (dash
lines). The two "X's" are design values from Reference 10.

Comparing the data (dots) to the design values in Figure 10, we see that:

>   the maximum receiver absorbed power is over 10% less
>   than predicted,

>   the predicted incident power at an absorbed power near the
>   experimental data is within the lower 95% prediction interval
>   calculated by the statistical method of evaluation.

This latter point implies, based on a single design value, that the predicted part load performance of the receiver is near the measured values, but the incident power for this value of the absorbed power is lower than the expected value from

the data, linear fit line. The difference between the data and prediction concerning this point will be shown to be in part accounted for by the difference between the actual measured solar absorptance and the value used for the design prediction.

Using the data, linear fit, and prediction interval from Figure 10, Figure 11 shows the steady state point-in-time receiver efficiency versus the receiver absorbed power. The dots, solid line, dashed lines, and X's have the same meaning as in Figure 10. From Figure 11 at an absorbed power of 34.0 MW_t, the expected receiver efficiency, linear fit line, is 76.7% with a 95% probability that the receiver efficiency will be between 72.9% and 80.8%. This expected value and 95% probability interval compares well with earlier test results from Reference 4 (1983) and Reference 5 (1985). There the receiver efficiency was reported to be near 76.0%. The predicted efficiencies from Reference 10 at an absorbed power of 34.2 MW_t and 40.8 MW_t are 81.2% and 81.9%, respectively. The predicted efficiency at the lower absorbed power is near the 95% probability interval shown in Figure 11 but on the high side. As will be shown, this difference in receiver efficiency between the design prediction and measured values can be accounted for in part by the receiver solar absorptance.
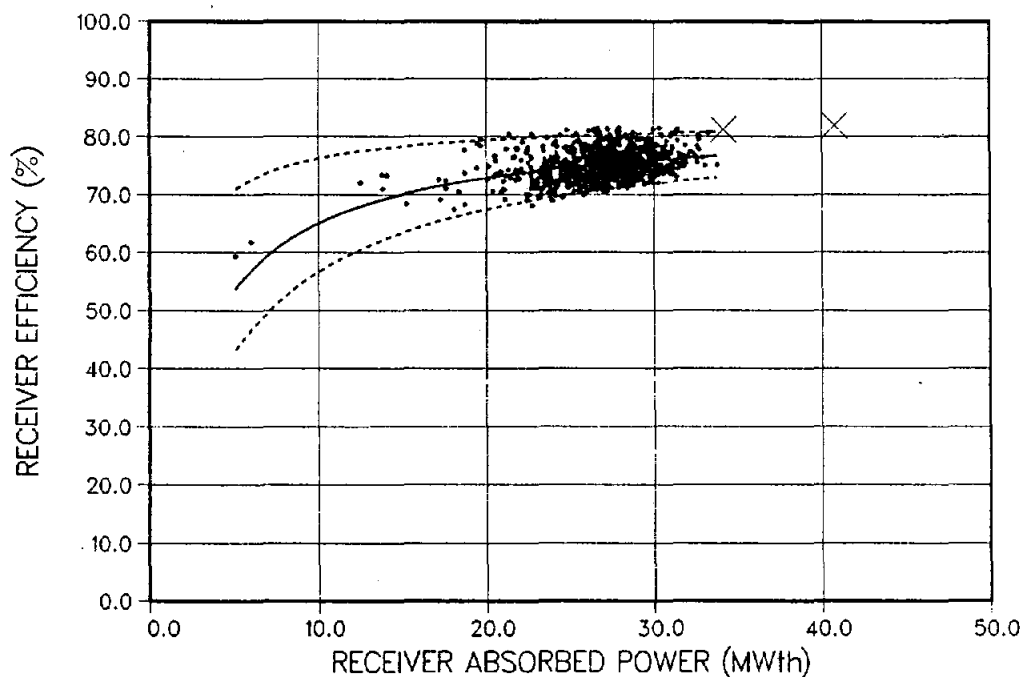
Figure 11. Calculated receiver efficiency versus calculated absorbed power data (dots), data fit (solid line), and 95% prediction interval (dash lines). The two "X's" are design values from Reference 10.

36

The maximum measured receiver absorbed power in Figure 11 is about 34 MW$_t$, and the expected value of the receiver efficiency from the linear fit line is 76.7%. The part load efficiency at three quarters of the maximum absorbed power, 25.5 MW$_t$, is 74.7% and at half load, 17.0 MW$_t$, is 71.4%. We see in Figure 11 that most of the steady state data is above the three quarters maximum value. Considering only insolation, the three quarters value of the reference point insolation, 973 w/m^2, would be about 730 w/m^2 and half about 487 w/m^2. The drop in receiver efficiency from maximum absorbed power, 76.7%, to half power, 71.4%, of just 5.3 percentage points is considered good since almost all receiver operation is above this value.

As indicated, during the design prediction of the performance of the receiver (Reference 10) the Pyromark paint covering the receiver absorber surface was assumed to have a solar absorptance of 0.95. We measured the receiver solar absorptance in November 1982 (month 11 - 0.92), December 1983 (month 24 - 0.90), and September 1984 (month 33 - 0.88) as reported in Reference 11. Months are counted from January 1982 with January 1982 being month 1. In addition to the measurements reported in Reference 11, we made solar absorptance measurements, using the techniques described in Reference 11, in March 1986 (month 51 - 0.97), August 1986 (month 56 - 0.97), and October 1987 (month 70 - 0.96). These last measurements were made after the receiver was over-coated, repainted, with Pyromark paint in December 1985 (month 48). Figure 12 shows the results of all of the solar absorptance measurements made on the Solar One receiver. The values shown in Figure 12 are the flat-surface-solar-absorptance values of the Pyromark paint on the receiver surface and can be compared to the value used for the design predictions. If we assumed that the solar absorptance degraded in a linear relationship with time as shown in Reference 11, then the solar absorptance in December 1985 before repainting the receiver would have been about 0.86. We see in Figure 12 that the month to month change in the solar absorptance after repainting is considerably less than before. We are still trying to understand the Pyromark paint degradation processes.

If we compare the measured flat surface values of the solar absorptance with the design prediction value, then the measured values are less than the design value by 3.1% (1982), 5.2% (1983), 7.3% (1984), and 9.5% (estimated 1985). Most of the data used in Figures 10 and 11 were from the latter part of 1983 through 1985 since plant operation improved with experience. Thus, part of the difference between the design prediction and data shown in Figures 10 and 11 can be accounted for by this difference in the receiver solar absorptance.

Another factor which may or may not have been included in the design prediction is the correct area of the receiver. We made measurements of the receiver circumference at the top, middle, and bottom. Based on these measurements we calculated an average receiver circumference. We also measured the receiver panel width and found that when all twenty-four panels are included the active receiver area is 3.8% less than the measured receiver exposed surface intercepted by the heliostat field reflected power. This means that the incident power calculated and
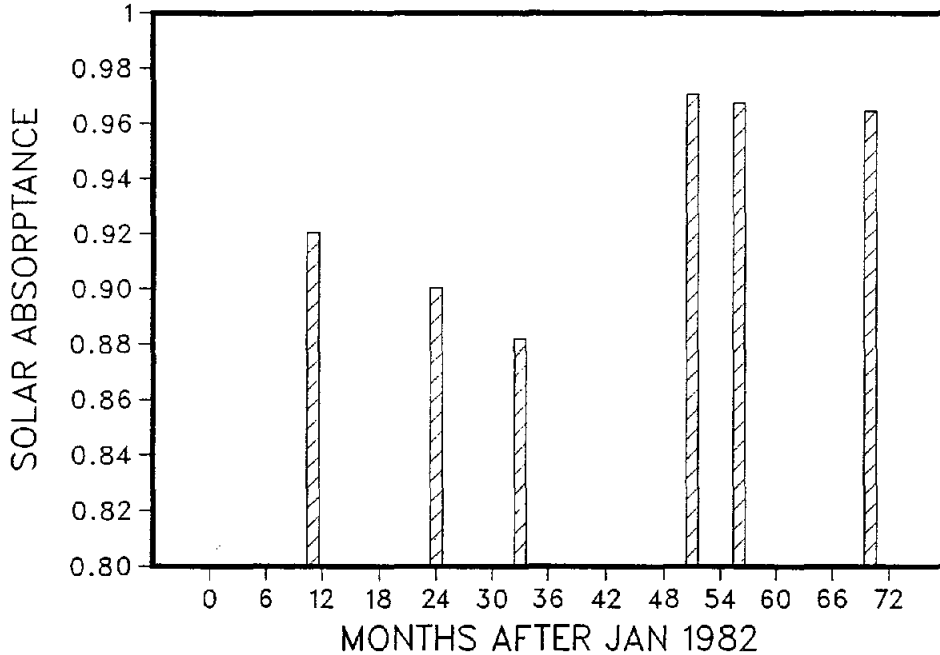
Figure 12. Solar absorptance measurement results from the Solar One receiver. These values are the flat surface solar absorptance measurements of the receiver Pyromark paint. The receiver was repainted in December 1985 (month 48).

used in Figures 10 and 11, which was for the exposed surface, was incident on 3.8% non-active surfaces and 96.2% active surfaces. This reduced receiver area also accounts for some of the difference between the design predictions and data in Figures 10 and 11. The approach to calculating the receiver incident power using the total receiver exposed surface is consistent with previous calculations. Present heliostat field performance codes cannot account for small gaps between receiver panels. The codes do account for the incident power on non-active surfaces at the top and bottom of the receiver and that power which misses the receiver at the major diameter. This power is considered as spillage.

Taking into account the active area of the receiver and the tube geometry of the panels, we calculated an effective receiver solar absorptance. Reference 12 gave the following equation to account for the tube geometry of the receiver panel,

$$Tube\ solar\ absorptance\ (\sigma_t) = \cfrac{1}{1 - \cfrac{2\left(1 - \frac{1}{\sigma_f}\right)}{\pi}} \qquad (3)$$

38

where "σ_f" is the measured flat surface solar absorptance and π equals 3.1416. For the Solar One receiver the effective solar absorptance (σ_{eff}) is then 96.2% of the tube solar absorptance (σ_t) to account for the reduced area from exposed to active. Table III gives the results from the measurement, tube solar absorptance, and Solar One receiver effective solar absorptance.

TABLE III
SOLAR ONE SOLAR ABSORPTANCE CORRECTIONS

Month	Measured Solar Absorptance (σ_f)	Tube Solar Absorptance (σ_t)	Effective Solar Absorptance (σ_{eff})
design	-	-	0.95
11	0.92	0.95	0.91
24	0.90	0.93	0.90
33	0.88	0.92	0.89
48	0.86 (est)	0.91	0.87
51	0.97	0.98	0.94
56	0.97	0.98	0.94
70	0.96	0.97	0.94

Recall that we made no measurement in December 1985 (month 48) and the value listed in Table III is an "estimate" from the equation in Reference 11. From Table III we see that the reduction in the effective solar absorptance from the first measurement, December 1982 to December 1985, is about 4.4%. We assumed that this reduction is within the uncertainty of the data used in Figures 10 and 11 and was not taken into account. However, the increase in the effective solar absorptance of 8.0% after repainting should be reflected in the data. This will be shown later in the report in the Receiver Thermal Loss section.

If we take into consideration the actual receiver solar absorptance and area factor, then the measured and predicted receiver point-in-time efficiencies are close. This indicates, at least for a surround external water/steam receiver, that design prediction can be in reasonable agreement with measured values.

To investigate the change in the receiver steady state point-in- time efficiency as a function of site wind speed, we used data from the steady state file. The procedure used was similar to that for the receiver incident versus absorbed power and efficiency versus absorbed power. In this case we used the same conditions as before on the receiver inlet and outlet temperature and outlet pressure. However,
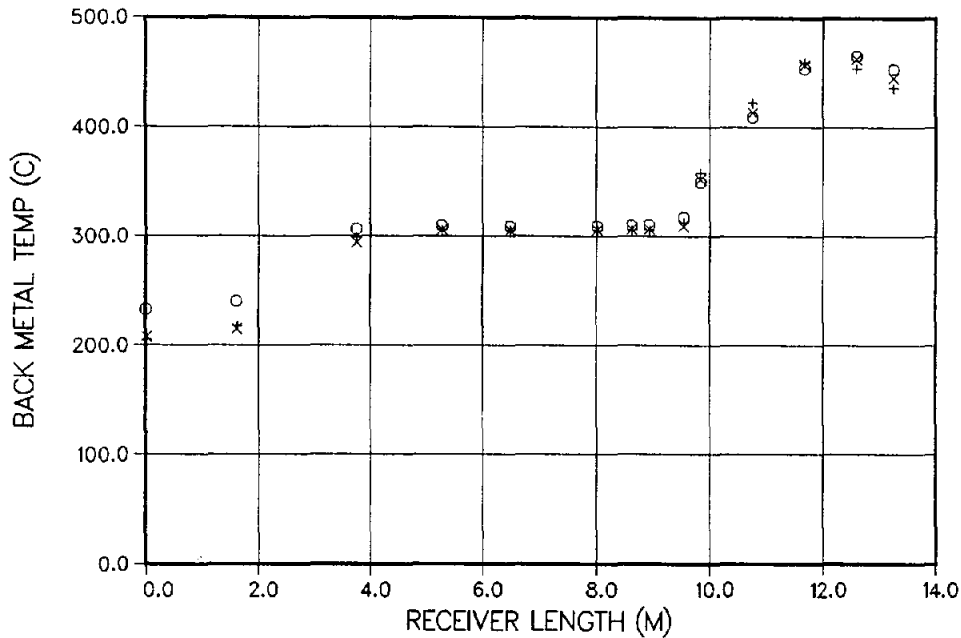
Figure 18. Receiver panel back surface temperature data during a thermal loss
test. The "x" and "+" are the two half power data, and the "o" is the
full power data.

fit for these same time intervals were the site insolation, receiver inlet and out-
let temperatures, wind speed, and ambient air temperature. We used Equation
(A-17) to find both the panel thermal losses and the receiver thermal loss.

Another parameter required for the solution of Equation (A-17), if it is not
assumed that the receiver thermal losses are independent of receiver power level,
is an estimate of the receiver thermal loss at each power level. These estimates
of thermal loss are used as a ratio of the thermal loss at each reduced power level
to the thermal loss at the full power level [see Appendix A Equations (A-14) and
(A-15)]. Two critical issues in making these estimates of thermal loss are the re-
ceiver front surface temperature during the test and the convection heat transfer
correlation. To make these estimates of the thermal loss at each power level, we
developed a simplified theoretical model of the receiver panels, see Appendix A,
to calculate the receiver panels front surface temperature. Knowing the front sur-
face temperatures from this model, we estimated the thermal loss.

The estimated thermal loss included only emitted radiation and convection
losses, we assumed the conduction loss negligible. Emitted radiation loss calcu-
lated for each panel was based on the average front surface temperature of the
three unique heat transfer regimes existing in the panels, i.e. subcooled water,
boiling, and superheated steam. The convection loss calculated was based on the

average receiver front surface temperature and a heat transfer correlation developed by Siebers (Reference 16). Another convection heat transfer correlation investigated was that by Siebers and Kraabel (Reference 17). One difference between these two correlations is that the Siebers correlation evaluates air properties at ambient temperature, and the Siebers and Kraabel correlation evaluates the forced convection correlation air properties at a film temperature. This film temperature is a function of both the ambient air temperature and front surface temperature. Since the front surface temperature is only estimated, preference was given to the Siebers correlation.

The investigation, before selecting the Siebers correlation, included calculating the receiver thermal loss using these two convection heat transfer correlations and comparing the results. The thermal loss calculation in this case used the detailed predicted front surface temperature distribution from Figure 7 for emitted radiation and an average front surface temperature for convection. Based on the thermal loss using each correlation, we calculated a receiver efficiency for various wind speeds using Equation (A-19). These efficiencies were normalized to give the same efficiency at a wind speed of 2 m/s as we determined in Figure 13, data fit line. Figure 19 shows the data fit line from Figure 13 and the results from the calculations using the two convection heat transfer correlations. We see in Figure 19 both correlations give nearly the same efficiencies, and both are slightly higher than the data fit line at the higher wind speeds. As was pointed out earlier, the data in Figure 13 did not consider wind speed effects on the receiver incident power and the efficiencies may actually be slightly higher at high wind speed. Thus, the selection of the Siebers correlation is justified although either correlation would have been acceptable.

To present the data from the thermal loss tests we defined the following nomenclature to use as headings in the tables:

TIME	-	solar time in hours (12.0 is solar noon)
INSOL	-	measured direct normal insolation
ABSPOW	-	calculated receiver absorbed power
TIN	-	measured receiver inlet water temperature
TOUT	-	measured receiver outlet steam temperature
HEL	-	number of heliostats tracking the receiver
WIND SP	-	measured wind speed
EFFIC FRACTION	-	receiver efficiency – as a fraction of the full power receiver efficiency
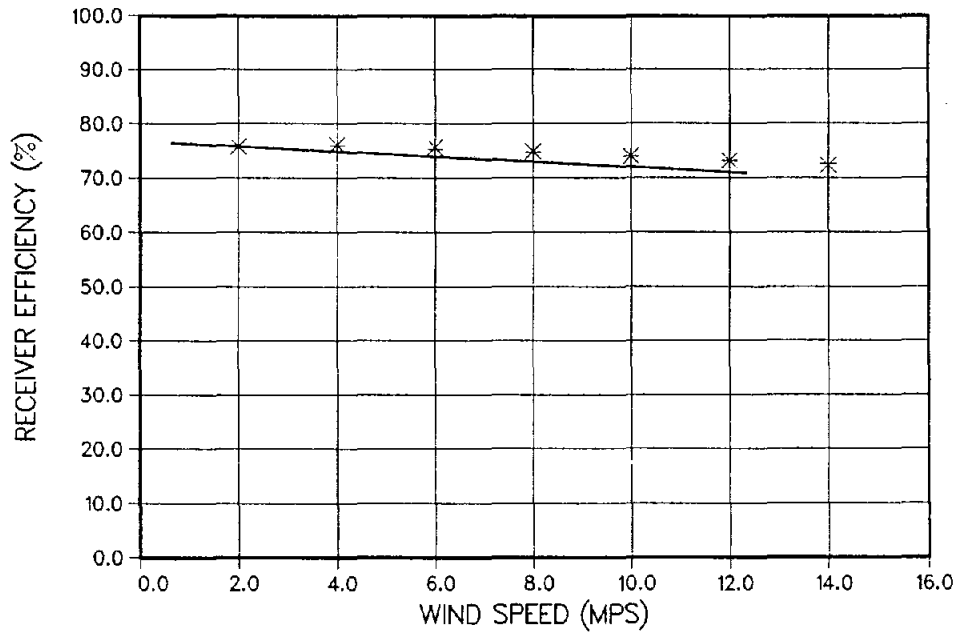
Figure 19. Receiver efficiency data fit line from Figure 13 (solid line) and efficiencies (normalized to give the same efficiency at 2 m/s) using the Siebers (-) and Siebers and Kraabel (x) convection heat transfer correlations.

One of the thermal loss tests was done before the receiver was repainted, October 31, 1985. Table VII gives data from this receiver thermal loss test.

TABLE VII

DATA FROM THE RECEIVER THERMAL LOSS TEST
ON OCTOBER 31, 1985

TIME	INSOL (w/m^2)	ABSPOW (MW_t)	TIN $(°C)$	TOUT $(°C)$	HEL	WIND SP (m/s)	EFFIC FRACTION
11.64	850.1	11.32	156.04	425.80	890	5.56	0.843
11.97	882.9	28.24	186.36	442.89	1802	4.41	1.000
12.31	904.7	13.46	159.13	430.96	917	4.92	0.914

Table VII shows that the insolation and wind speed were not constant during the test. This shows the importance of using Equation (A-17) in Appendix A for calculating the thermal loss since this equation accounts for changes in these parameters. The results in Table III show that the receiver effective solar absorptance for October 31, 1985, was 0.878.

54

We used Equation (A-17) to calculate the thermal loss from each receiver boiler panel and the combined preheat panels. For the boiler panels we used the panel inlet and outlet temperatures and pressures and panel flow to calculate the panel absorbed power. The preheat panels were combined to calculate the absorbed power for all preheat panels. These panel thermal losses were added giving a total thermal loss at the full power level of 3.959 MW_t. Also, we used Equation (A-17) to calculate the thermal loss for the receiver. For this case we used the receiver inlet and outlet temperatures and pressures and total receiver flow to calculate the receiver absorbed power. The resulting receiver thermal loss at full power, measured loss, is 4.360 MW_t. Appendix B gives the results of an uncertainty analysis we performed for the thermal loss tests. The root-sum-square of the receiver thermal loss precision and bias errors is $\pm$ 1.28 MW_t, Appendix B. The receiver thermal loss is nearly the same as the sum of the panels thermal loss.

We assume the receiver thermal loss is more accurate since the total receiver flow used included data from both the receiver and panels and is more accurate than an individual panel flow. The measured thermal loss, 4.360 MW_t $\pm$ 1.28 MW_t, is slightly less than that calculated from the statistical method of least squares, 4.74 MW_t with an estimated standard deviation of 1.2 MW_t, shown in Figure 14. When we consider the errors in both methods of determining the thermal loss, the results are the same. However, the thermal loss test was done on one day while the statistical method used data from many days to get the same nominal value of the thermal loss. For a receiver which will be operated for only a limited amount of time the thermal loss test is a method to get loss data.

The solution of Equation (A-17) requires an estimate of the panel or receiver thermal loss at both the part and full power levels. We used the sum of Equations (A-24), (A-25), and a fraction of (A-27) for the estimate of the panel thermal loss and Equation (A-28) for the estimate of the receiver thermal loss. These estimates used measured absorbed powers to calculate the panel front surface temperatures, see Appendix A, rather than the incident power which is normally used by designers. The result from Equation (A-28) for the estimate of the receiver thermal loss at full power, predicted loss, is 3.630 MW_t. This receiver predicted loss is 83.3% of the measured loss at full power. Results from Equation (A-28) for the part power levels showed the part power predicted thermal loss is about 87.6% of the full power predicted loss. Again, this shows the importance of using Equation (A-17) in calculating the measured thermal loss since it accounts for changes in the part power loss estimates.

A summary of the results of the calculations for the different thermal losses from the data in Table VII are:

Sum of the panel measured thermal losses   -   3.958 MW_t

Receiver measured thermal loss   -   4.360 MW_t $\pm$ 1.28 MW_t

Predicted receiver thermal loss   -   3.630 MW_t

We calculated the receiver efficiency using Equation (A-19) for both the predicted and measured full power losses. The receiver efficiency using the predicted loss is 77.8% and the measured loss is 76.1%. If we use the receiver measured loss, the root-sum-square of the receiver efficiency precision and bias errors is ± 2.57%, Appendix B.

The predicted loss which is 83.3% of the measured loss gives a receiver efficiency which is only 2.2% higher than the measured loss efficiency. In this case a 20% difference in thermal loss results in only a 2% difference in receiver efficiency. We used Equation (A-5) to calculate the fraction of the full power efficiency for each of the part power levels. These results are shown in the last column of Table VII. We see from this last column that the receiver efficiency at part power, less than half of the absorbed power, is over 84% of the efficiency at full power. Note that the wind speeds during the part power portions of the test are higher than at full power.

The efficiency results from the measured thermal loss data are compared to the results of the statistics method of least squares in Figure 20. Figure 20 shows the receiver efficiency data fit line (solid line) and prediction interval (dash lines) from Figure 11 compared to the efficiencies from the thermal loss test ($\otimes$). The two "X's" are design values from Reference 10. The data in Figure 11 was collected before the receiver was repainted. We see from Figure 20 the results from the thermal loss test are nearly the same as the expected value, data fit line, of the receiver efficiency from the method of least squares. Both the peak value of the efficiency and part power values follow the trend in the efficiency as a function of receiver absorbed power determined from Equation (1) using the least squares method of evaluation. Thus, by using a different method to evaluate the receiver efficiency, independent of the receiver incident power, the same results were found before the receiver was repainted.

The receiver incident power value for the thermal loss test was not needed for the evaluation of the losses. However, it was calculated for the full power case for information. The receiver efficiency using the absorbed and incident powers for this case was 71.8%. We see from Figure 20 that this value of the receiver efficiency would lie on the lower 95% prediction interval line. This agrees with the definition of the prediction interval; given a value of the receiver absorbed power, there is a 95% probability that the receiver efficiency will be within the prediction interval.

A summary of the results of the calculations for the different receiver efficiencies from the data in Table VII and incident power calculation are:

Receiver efficiency for the measured thermal loss - 76.1% ± 2.57%

Receiver efficiency for the predicted thermal loss - 77.8%

Receiver efficiency using incident power - 71.8%
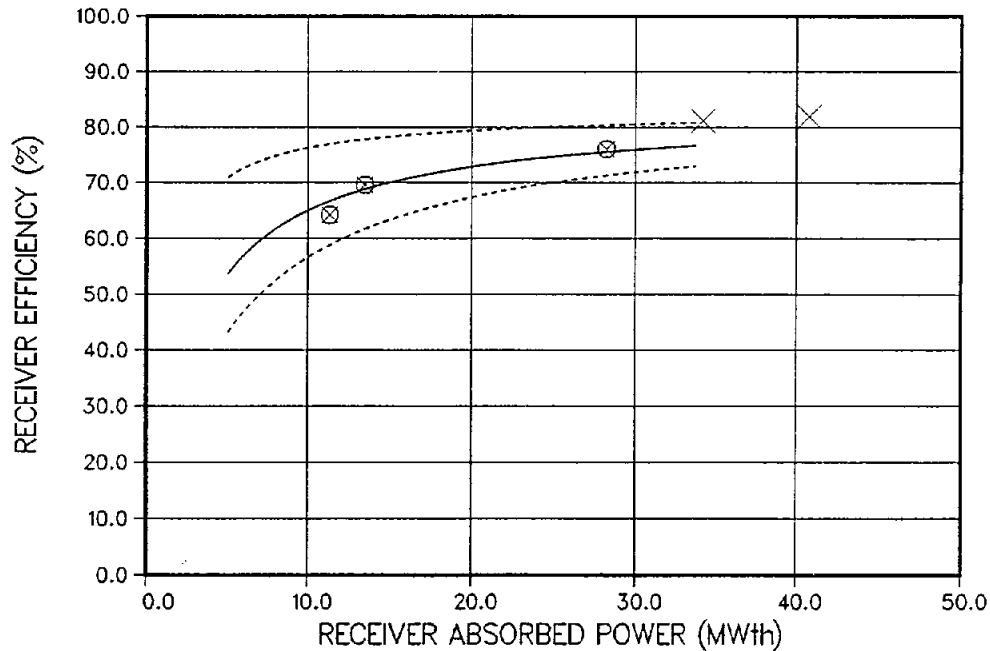
Figure 20. Receiver efficiency data fit line (solid line) and prediction interval (dash lines) from Figure 11 compared to the efficiencies from the thermal loss test (⊗) on October 31, 1985. The two "X's" are design values from Reference 10.

We performed two thermal loss tests after the receiver was repainted. These tests were done in March 1986. Table VIII shows the data from the thermal loss test on March 19, 1986.

TABLE VIII

DATA FROM THE RECEIVER THERMAL LOSS TEST
ON MARCH 19, 1986

TIME	INSOL (w/m^2)	ABSPOW (MW$_t$)	TIN (°C)	TOUT (°C)	HEL	WIND SP (m/s)	EFFIC FRACTION
11.48	979.2	16.10	162.22	421.37	880	3.90	0.889
11.97	982.7	36.96	188.97	420.29	1790	3.61	1.000
12.48	980.2	16.87	162.98	421.73	913	5.73	0.894

The receiver effective solar absorptance for March 19, 1986, was 0.937 from the data in Table III after the receiver was repainted. In this test the direct normal

insolation was nearly constant during the test and higher than for the test in October 1985. As a result of the higher insolation the receiver absorbed power for each power level was higher.

We used the same equations and procedures to calculate the different thermal losses from the data in Table VIII as we used for the data in Table VII. A summary of the results of the calculations for the different thermal losses from the data in Table VIII are:

Sum of the panel measured thermal losses - 5.035 MW$_t$

Receiver measured thermal loss - 4.914 MW$_t$ ± 0.48 MW$_t$

Predicted receiver thermal loss - 3.728 MW$_t$

The root-sum-square of the receiver measured loss precision and bias errors is ± 0.48 MW$_t$, Appendix B. As was the case for the data in Table VII, the sum of the panel measured thermal losses and the receiver measured thermal loss are nearly the same. We again assume the receiver measured thermal loss is more accurate. In this case the measured thermal loss, 4.914 MW$_t$, is higher than that found in October 1985, 4.360 MW$_t$. Part of the difference between the two measured loss tests can be accounted for by the higher absorbed power causing higher front surface temperatures. The predicted receiver thermal loss for March 19 is 75.8% of the measured thermal loss compared to 83.3% for the data in Table VII. This indicates the model does not accurately describe the front surface temperatures or losses. However, the model is used only to calculate the ratio of the losses at part power to the loss at full power required for the solution of Equation (A-17).

A summary of the results of the calculations for the different receiver efficiencies from the data in Table VIII and incident power calculation are:

Receiver efficiency for the measured thermal loss - 82.7% ± 0.65%

Receiver efficiency for the predicted thermal loss - 85.1%

Receiver efficiency using incident power - 81.7%

The root-sum-square of the receiver efficiency, using the receiver measured loss, precision and bias errors is ± 0.65%, Appendix B. The receiver efficiency, using the measured thermal loss for March 19, after the receiver was repainted, is about 8% higher than that found in October 31, before repainting. This increase in receiver efficiency is nearly the same as the increase in effective solar absorptance after repainting the receiver. Even though the predicted thermal loss is about 75% of the measured thermal loss, the receiver efficiency is only 3% more. Again, this shows the relative insensitivity of the receiver efficiency to small differences

in the calculated receiver thermal loss. For the data in Table VIII, the receiver efficiency using the incident power, Equation (1), is about the same as that from the measured thermal loss, Equation (A-19), independent of incident power. The data in the last column of Table VIII shows that the part power efficiency – as a fraction of the full power efficiency – is about 89%.

The last thermal loss test we performed was on March 20, 1986. Table IX shows the data from that test.

TABLE IX

DATA FROM THE RECEIVER THERMAL LOSS TEST
ON MARCH 20, 1986

TIME	INSOL (w/m^2)	ABSPOW (MW$_t$)	TIN (°C)	TOUT (°C)	HEL	WIND SP (m/s)	EFFIC FRACTION
11.51	980.5	15.97	161.25	436.16	880	4.43	0.891
12.01	983.8	36.70	199.73	434.00	1796	4.42	1.000
12.51	980.6	16.55	163.31	436.56	916	5.32	0.887

The receiver effective solar absorptance is the same as for March 19, 1987. The direct normal insolation on March 20 was about the same as that on March 19 and higher than that for October 1985. The receiver absorbed powers for March 20 are similar to those on March 19. Receiver outlet steam temperatures on March 20 were about 15 °C higher than on March 19.

We used the same equations and procedures to calculate the different thermal losses as before. A summary of the results of the calculations for the different thermal losses from the data in Table IX are:

Sum of the panel measured thermal losses   - 5.740 MW$_t$

Receiver measured thermal loss   - 5.564 MW$_t$ $\pm$ 2.33 MW$_t$

Predicted receiver thermal loss   - 3.915 MW$_t$

The root-sum-square of the receiver measured loss precision and bias errors is $\pm$ 2.33 MW$_t$, Appendix B. The measured thermal loss for March 20, 5.564 MW$_t$, with its higher steam outlet temperature, is higher than that for March 19, 4.914 MW$_t$. It is doubtful that this difference in thermal loss is attributable to the increased outlet temperature. The error analysis for this test, Appendix B, shows the largest errors for the thermal loss tests. For the March 20 data, the predicted thermal loss is only 70% of the measured loss.

A summary of the results of the calculations for the different receiver efficiencies from the data in Table IX and incident power calculation is:

Receiver efficiency for the measured thermal loss   - 81.4% ± 4.13%

Receiver efficiency for the predicted thermal loss   - 84.7%

Receiver efficiency using incident power   - 81.0%

The root-sum-square of the receiver efficiency, using the receiver measured loss, precision and bias errors is ± 4.13%, Appendix B. These efficiency results are similar to those from March 19. The difference between the measured and predicted thermal loss efficiencies for March 20, 4%, reflects the 70% difference between the measured and predicted losses. The part power efficiencies – as a fraction of the full power efficiency – in Table IX, are about the same as those in Table VIII. The efficiency calculated with the incident power is the same for March 19 and March 20 for the same absorbed powers.

To show the increase in the receiver efficiency after repainting the receiver, we compared the efficiencies using the receiver measured thermal loss data for March 19 and 20 to that shown in Figure 11. Figure 21 shows the receiver efficiency data fit line (solid line) and prediction interval (dash lines) from Figure 11 compared to the efficiencies from the thermal loss tests ($\otimes$) on March 19 and 20, 1986. The two "X's" are design values from Reference 10. We see in Figure 21 the receiver efficiencies after repainting the receiver are higher than those before repainting. These latest efficiencies are nearly the same as the design values from Reference 10. After repainting the receiver, the measured flat surface solar absorptance was the same as that used for the design prediction of efficiency. The trend in the receiver efficiency as a function of absorbed power is the same as before repainting with the after repainting data being higher.

The three thermal loss tests gave receiver measured thermal losses ranging from 4.4 MW$_t$ to 5.6 MW$_t$. The error analysis in Appendix B for the measured losses shows the precision errors ranged from 0.3 to 2.3 MW$_t$, and the bias errors ranged from 0.4 to 0.7 MW$_t$. These values of measured loss are of the same order as that found from the statistical method of least squares, about 4.7 MW$_t$ with an estimated standard deviation of 1.2 MW$_t$, shown in Figure 14. All of these thermal loss values determined from the experimental data are near that predicted by the receiver designer in Reference 10 for higher receiver outlet steam temperatures. Although much is still to be learned about the details of receiver thermal losses, this data shows that predictions are of the same order as measured data.

The receiver efficiency using the measured thermal loss data, Equation (A-19), before repainting the receiver was nearly the same as that found using the statistical method of least squares, Equation (1). The efficiencies after repainting were higher than before repainting by about the same amount as the increase in the effective solar absorptance. After repainting, when the solar absorptance was

60
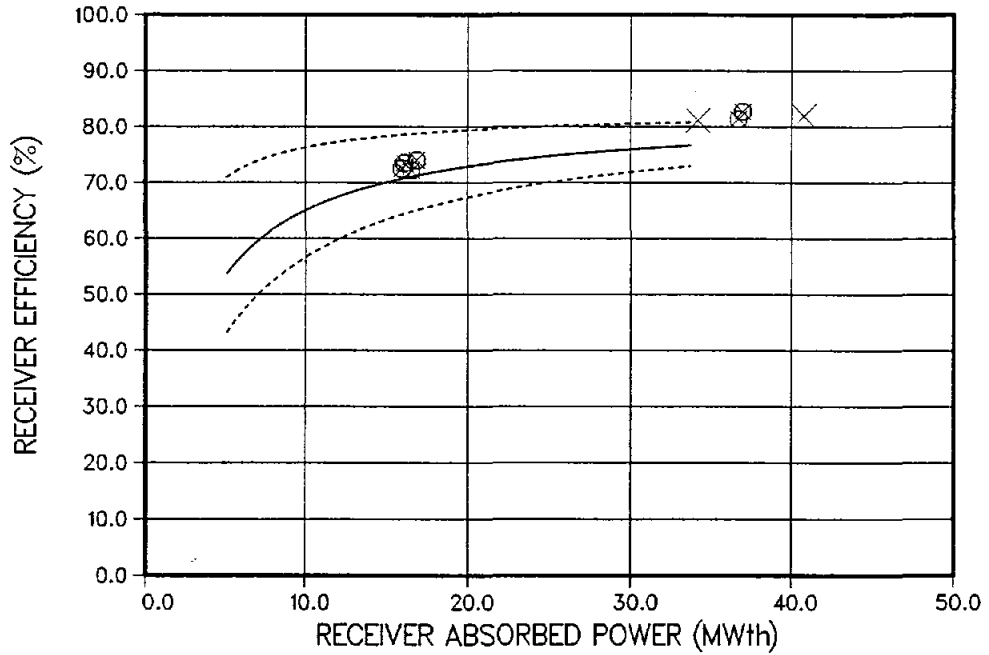
Figure 21. Receiver efficiency data fit line (solid line) and prediction interval (dash lines) from Figure 11 compared to the efficiencies from the thermal loss tests ($\otimes$) on March 19 and 20, 1986. The two "X's" are design values from Reference 10.

the same as that used by the receiver designers, the receiver efficiency was about the same as the design prediction, Reference 10.

Cloud Transients

It is difficult to quantify in exact terms receiver operation during cloud transients. However, how well the receiver can operate during cloud transients will directly affect the amount of solar energy the receiver collects. The approach we took for this evaluation was to examine data plots of receiver operation during cloud transients and draw general conclusions about how well the receiver operated through the cloud transients examined. We used data for this evaluation from the summary data tapes recorded at three minute time intervals so there may be insolation changes occurring that are not known. Reference to time is in minutes from midnight. The parameters we considered are site solar insolation, number of heliostats tracking the receiver, and the receiver outlet steam temperature. As mentioned in the Receiver Description section, each panel has three flux gages mounted at different elevations at the center of the panel. To further understand how clouds affect the receiver, we examined data from panel flux gages representing four quadrants of the receiver, southeast (SE), northeast (NE), northwest (NW), and southwest (SW). Thus, when the site insolation changed, we could see if similar changes occurred on the various quadrants of the receiver.

For future comparison with data of operation during cloud transients, a plot for a clear day is shown in Figure 22. Figure 22 shows that all available heliostats began tracking the receiver just after sunrise; insolation was about 150 w/m^2 and the time was 377 minutes. As the insolation increased, the receiver outlet temperature increased through its sequence of set temperatures, pausing first at just over 200°C and again at over 300°C; reaching a final outlet temperature of 415°C when the insolation reach 750 w/m^2. The receiver outlet temperature remained nearly constant throughout the day until the insolation decreased to about 600 w/m^2. When the insolation reached about 600 w/m^2, the operator began to decrease the receiver outlet temperature until it was below 315°C; then he removed the heliostats tracking the receiver, 1146 minutes and insolation below 150 w/m^2 in Figure 22. The four quadrants of the receiver had similar, but reduced, profiles of insolation as did the site insolation during heliostat tracking of the receiver.

Figure 23 shows a case where the receiver start-up was delayed from sunrise and began at an insolation value of 470 w/m^2, 380 min, when most available heliostats began tracking the receiver. We sequenced through the set receiver start-up temperatures. Because of the flow limitation of the receiver flash tank, the number of heliostats tracking the receiver had to be reduced until the downcomer could be conditioned and superheated steam flow was directed to the downcomer. After that was completed, the receiver was operating as it would on a clear day, Figure 22. At about 600 minutes, Figure 23, a cloud transient caused a significant change in the magnitude of the site insolation, 98.0%. The heliostat reflected solar flux density on the southwest (SW) quadrant of the receiver reduced 75.0%, northwest (NW) 91.0%, northeast (NE) 37.0%, and southeast (SE) 0.0%. Within one data tape time step, 3 minutes, the site insolation was back at the clear day

62
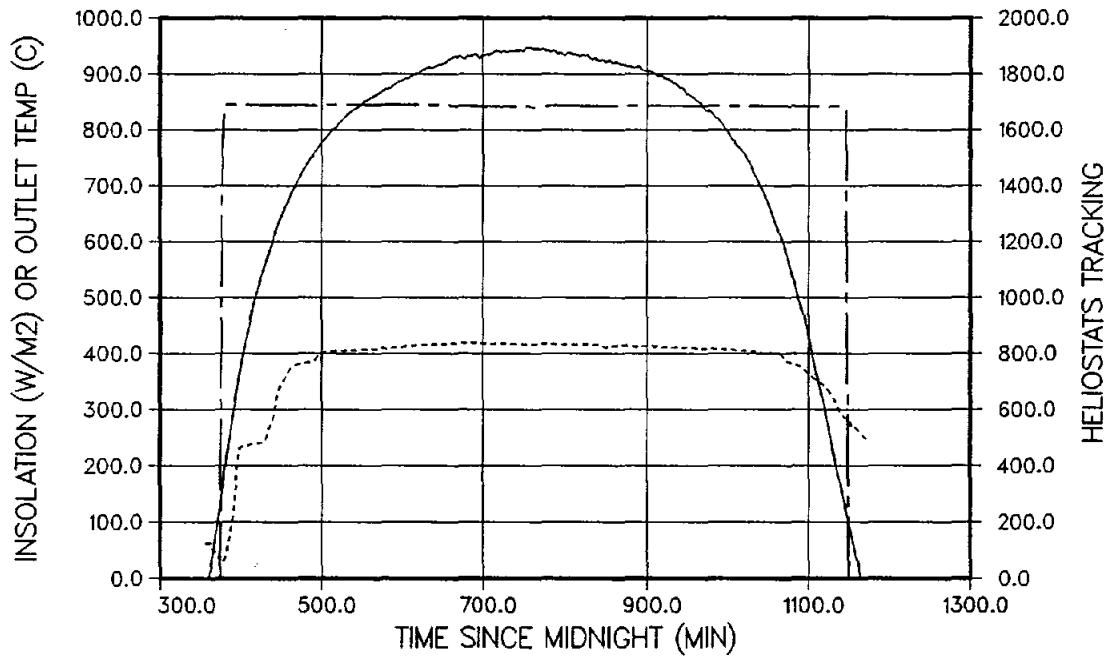
Figure 22. Clear day receiver operation data showing site insolation (solid line), receiver outlet steam temperature (small dash line), and number of heliostats tracking the receiver (long dash line).

Figure 23. Receiver operation after start-up with intermittent cloud transients showing site insolation (solid line), receiver outlet steam temperature (small dash line), and number of heliostats tracking the receiver (long dash line).

value. Since each boiler panel has its own flow control valve to control the panel outlet temperature, the receiver outlet temperature swing was only about 4.0%. Since not all of the receiver quadrants were affected by the cloud, the receiver total flow decreased only about 30% and the plant steam turbine continued operation. After this cloud passed the receiver had over 20 minutes of clear day operation before the next cloud.

At 633 minutes, Figure 23, another cloud caused an 87.0% decrease in site insolation. Again not all receiver quadrants were affected the same by this decrease in site insolation, SW 26%, NW 88%, NE 44%, and SE 18%. Total receiver flow decreased about 34%, and the turbine continued operation. Again this cloud transient was one data tape time step in duration. About 9 minutes later, 645 minutes, another cloud transient of longer duration caused a maximum decrease in site insolation of 94% with each receiver quadrant flux density decreasing around 80%. The total receiver flow decreased about 90% from that before the cloud, and the turbine was taken out of operation. The receiver continued operation after the cloud passed with outlet temperature oscillation of $\pm$ 9%.

In general, the insolation shown in Figure 23 seemed to drop and rise very quickly, except on one occasion at 645 minutes, and then stay nearly constant for a few minutes. The rapid 50% to 90% reductions and increases in the insolation did cause the receiver outlet temperature to oscillate a few degrees around its nominal value. At 645 minutes in Figure 23, the large drop in insolation was not followed by an immediate increase and the outlet temperature showed its largest oscillation, and the turbine was shut down. Late in the afternoon, 885 minutes, the insolation decreased to 0.0 w/m^2 (100%) with each receiver quadrant experiencing similar decreases. This zero insolation lasted two data tape time steps, 6 minutes, and the receiver outlet temperature dropped over 100°C (30%). When the insolation increased back to its original value the receiver outlet temperature increased 100°C (30%) over its nominal value of 410°C. Within another 6 minutes the insolation decreased again, this time for 9 minutes, and the receiver was shut down, heliostats removed from tracking. This case showed that if the site insolation change was of short duration and had a small time delay between significant changes in insolation, although they may continue to occur, the receiver outlet temperature changes are small. However, at Solar One with the steam direct from the receiver to the turbine, if the total receiver flow is reduced significantly, the turbine will be taken out of operation.

Figure 24 shows a case of early morning start-up with low insolation and cloud transients which lasted until after noon. This case has a high frequency insolation oscillation along with a low frequency oscillation of the mean value of the insolation. Each quadrant of the receiver had similar oscillations in its solar flux density. Initially over half of the heliostats began tracking the receiver and then even more were put in track. The outlet temperature began to increase through its start-up sequence but at a slower rate because of the low insolation. During this start-up, changes in insolation of $\pm$ 50% of a nominal 150 w/m^2 were occurring and the outlet temperature was oscillating. During this phase of the receiver

64

start-up, the receiver flow is constant, so the outlet temperature will change with insolation. As the insolation began to increase, so did the outlet temperature. When the outlet temperature reached about 240°C, 508 minutes, a few heliostats were removed from tracking to reduce the total receiver flow until the receiver reached a steam condition and the downcomer is opened.
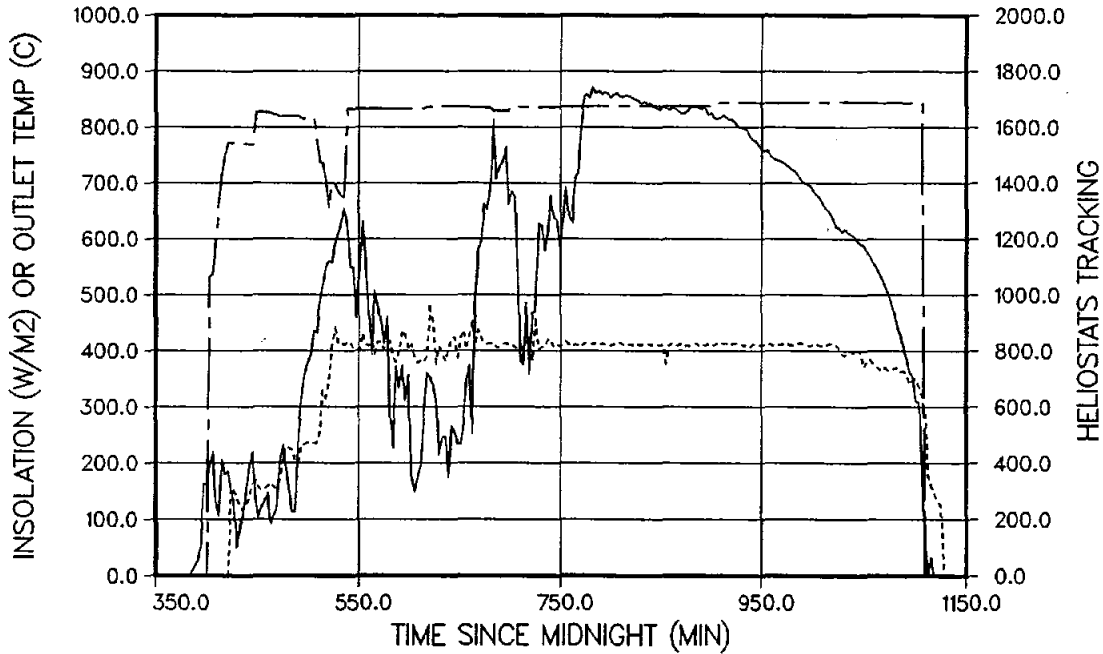
Figure 24. Receiver operation with cloud transients during morning start-up show-
ing site insolation (solid line), receiver outlet steam temperature (small
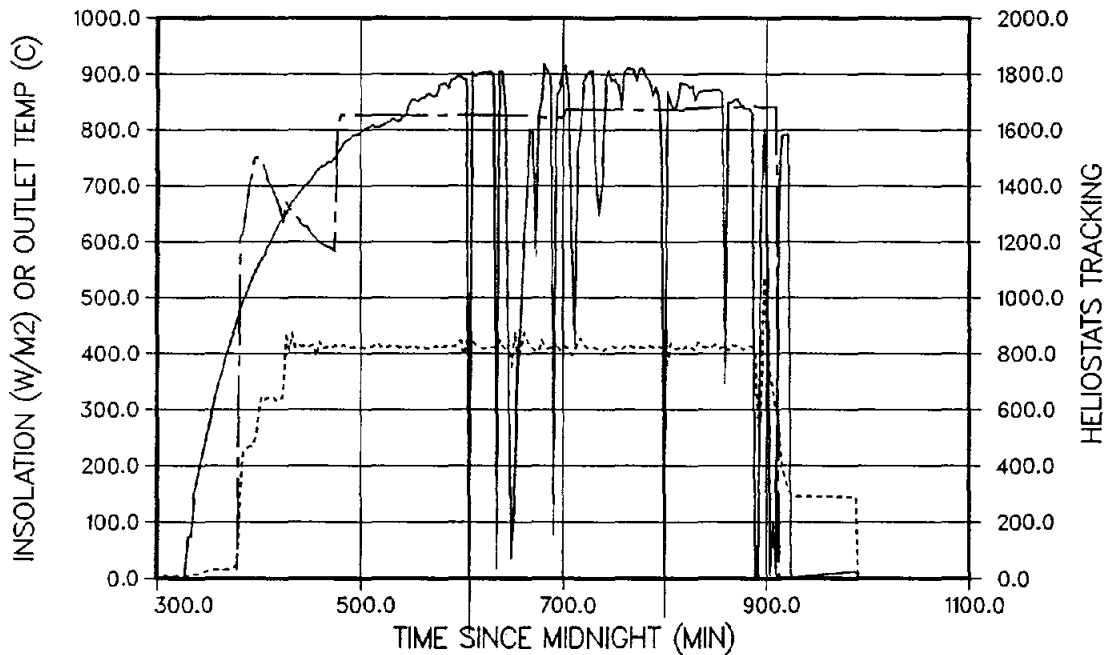dash line), and number of heliostats tracking the receiver (long dash
line).

Once the downcomer was open, all heliostats were put in track and receiver flow was changed to maintain a set outlet temperature. The insolation began to decrease, 540 minutes Figure 24, with some oscillation and the outlet temperature began to oscillate. When the insolation reached about 300 w/m^2, there was a decrease to 150 w/m^2, 605 minutes, followed by an increase to over 300 w/m^2. The outlet temperature peaked at around 484°C, 620 minutes, on the increase in insolation before it returned to near 410°C with smaller oscillations. Each receiver quadrant was experiencing similar changes in its solar flux density. The increase in insolation from 300 w/m^2 to over 750 w/m^2, 683 minutes, had very little effect on the outlet temperature. A decrease in insolation from 750 w/m^2 to 375 w/m^2, 710 minutes, caused the outlet temperature to oscillate. The subsequent increase in the insolation to over 800 w/m^2, 770 minutes, again had little effect on the outlet temperature. At this time large changes in the insolation stopped, and the rest of the day was similar to that shown in Figure 22. For the case shown in Figure 24, an overall reduction in the insolation with oscillations seems to have a greater effect on the receiver outlet temperature than an overall increase with oscillations. When the insolation decreases, the receiver flow also decreases, and

insolation oscillation at low flow condition seems to affect the receiver outlet temperature more than at high flows.

Figure 25 shows a case where, after a typical clear day start-up (Figure 22) and the receiver outlet temperature had reached its nominal 415°C value, there was a large, 80%, decrease in the insolation. Each receiver quadrant had decreases of 69% (SW), 26% (NW), 20% (NE), and 80% (SE) in solar flux densities. However, the receiver quadrants NW, NE, and SE continued to stay low or go even lower, all near 60%, even though the site insolation increased back to around 775 w/m². This reduced flux density on these three receiver quadrants caused the total receiver flow to reduce, and the turbine was taken out of service. The site insolation then began a series of large and continuous changes, starting at 595 minutes, lasting for several minutes. Heliostats were removed from tracking the receiver to try to keep the receiver in operation, but this failed and the receiver was shut down at 604 minutes. After several minutes the insolation became more constant, and a mid day receiver start-up was initiated. During this receiver start-up the insolation again began to have large and continuous changes and the start-up was aborted. This case shows that large and continuous changes in the insolation, with almost no time delay between the changes, will force the receiver to shut down if it is operating and also, the receiver can not sequence through its start-up with such large and continuous changes in the insolation.
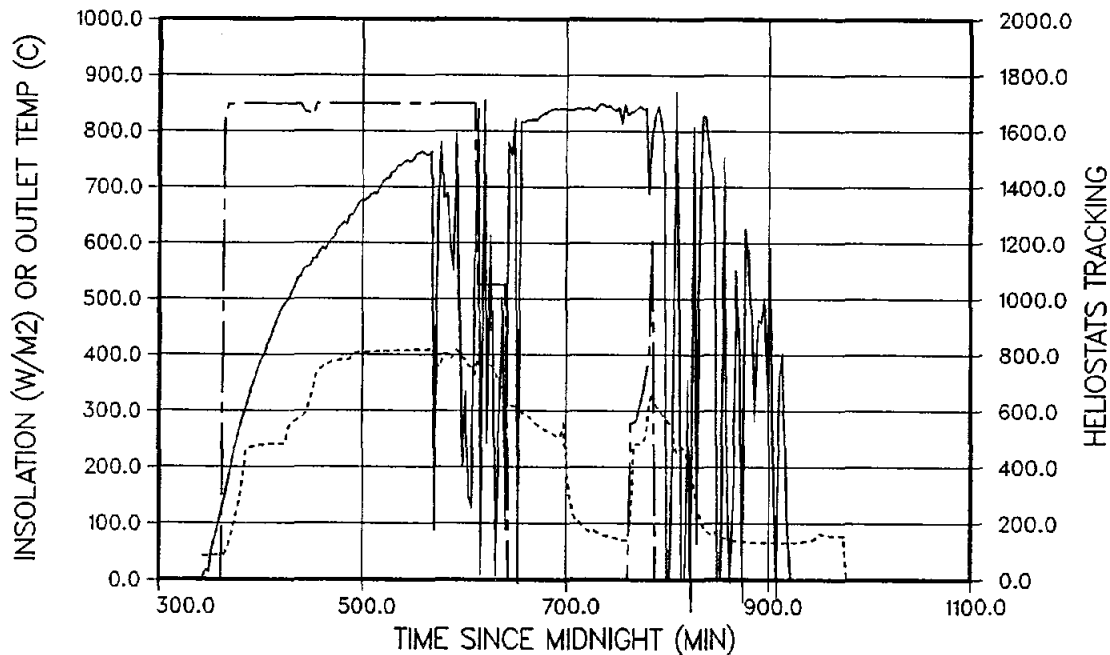
Figure 25. Receiver operation after normal start-up with cloud transients having large and continuous changes showing site insolation (solid line), receiver outlet steam temperature (small dash line), and number of heliostats tracking the receiver (long dash line).

66

These three cases of receiver operation during cloud transients, each having its own characteristics, demonstrate a range of cloud transients for the receiver at Solar One. Only large and continuous changes in the insolation with very small time intervals between the changes kept the receiver from operating (Figure 25). After the receiver has completed its start-up, it can operate through large changes in the insolation if there is some time delay between these changes (Figures 23 and 24). This is in part because each boiler panel flow control valve will control the flow through its panel to maintain its set outlet temperature. Cloud transients even at low insolation with some time delay between insolation changes did not keep the receiver from starting up or keep it from operating (Figure 24).

Even though the receiver could operate through cloud transients with large changes in insolation, which result in large changes in water/steam flow through the receiver, the turbine/generator set could not continue to operate. Also, associated with these changes in insolation, the receiver tube metal temperature is experiencing high ramp rate increases and decreases. These temperature changes could affect the receiver life by low cycle fatigue and the panel structures by high thermal stresses.

Receiver Life

Receiver life includes the performance of the panel mechanical supports and the occurrence of panel tube leaks. The continuous operation of the Solar One receiver since early February 1982, when the sun's reflected energy was first incident on the receiver, has provided an opportunity to evaluate receiver life. The receiver has been in operation seven days a week, from sunrise to sunset, for five years, except when weather or hardware problems limited operation.

The Solar one receiver is designed to have a 30-year life. All twenty-four receiver panels are the same design. The only differences between the panels are the inlet orifices and instrumentation. The panels are designed to be flat in the vertical direction , see Figure 8, and have a radius of curvature equal to the receiver radius in the lateral direction.

A 70-tube receiver panel consists of seven subpanels of ten tubes. The subpanel tubes are welded together along their entire length; then the subpanels are welded together. Attachments are welded on the back of the panel to carry the panel loads. Figure 26, a schematic of a receiver panel, shows the tube bends at the top and bottom of the panels (a), the inlet and outlet manifolds, panel module support, and the panel support at levels 1-6 (b). The weight of the panel is carried by supports under each subpanel at the top of the panel, level 7 in Figure 26. After the subpanel tubes are welded together, the tube ends are bent to an appropriate shape. The first bend at both the top and bottom is approximately a 90° bend toward the core or inside of the receiver with about a 38 mm bend radius, diagram (a) in Figure 26. The lengths of the subpanels and the tube shapes
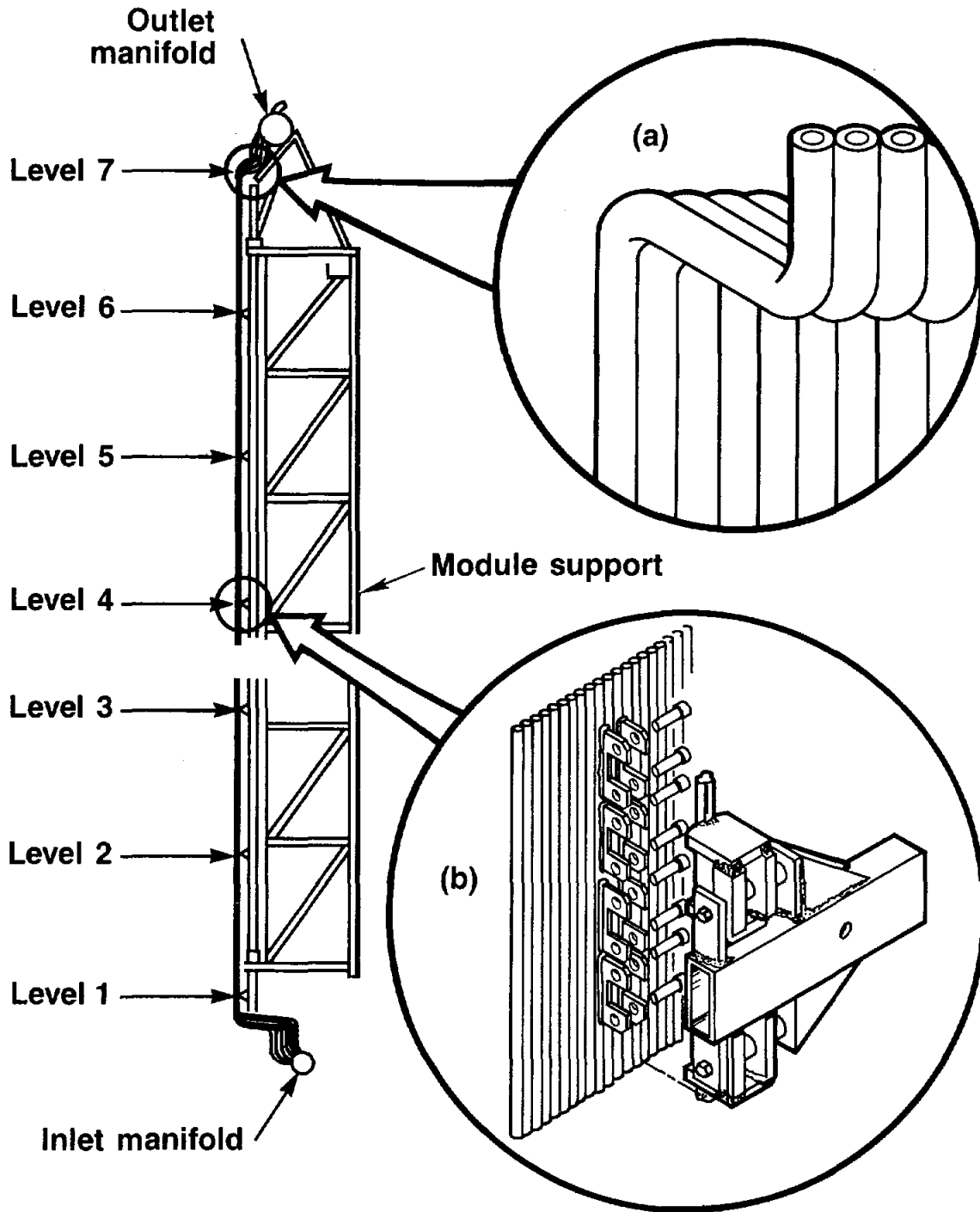
Figure 26. A schematic of a receiver panel showing the tube bends at the top and bottom of the panels (a), inlet and outlet manifolds, module support, and panel supports at levels 1-6 (b). The level 7 support is fixed and supports the weight of the panel.

after the first bend on each end are different to allow the tubes to be welded to the panel inlet and outlet manifolds.

The welds between the subpanels are referred to as the panel "interstice welds". An interstice weld is terminated at the top and bottom of the panel by extending the weld along the shortest subpanel and wrapping it over about one inch on the front of the panel. The small portion of insulation at the top and bottom of the panel cover the interstice weld termination. Figure 27, a photograph of the top portion of a panel, shows the subpanels (a), supports under the subpanel first 90° bend (b), and interstice welds on the front of the panel (c). The insulation at the top of the panel has been removed to expose this area of the panel. We can see in Figure 27 the different lengths of the subpanels (a) and the supports at level 7 (shown in Figure 26), under each subpanel (b), which carry the weight of the panel. The interstice weld termination between subpanels, one inch long welds on the front of the panel, can be seen in Figure 27 (c). The wires in Figure 27 across the top of the subpanels are used to hold the insulation, white material above the subpanels, in place.
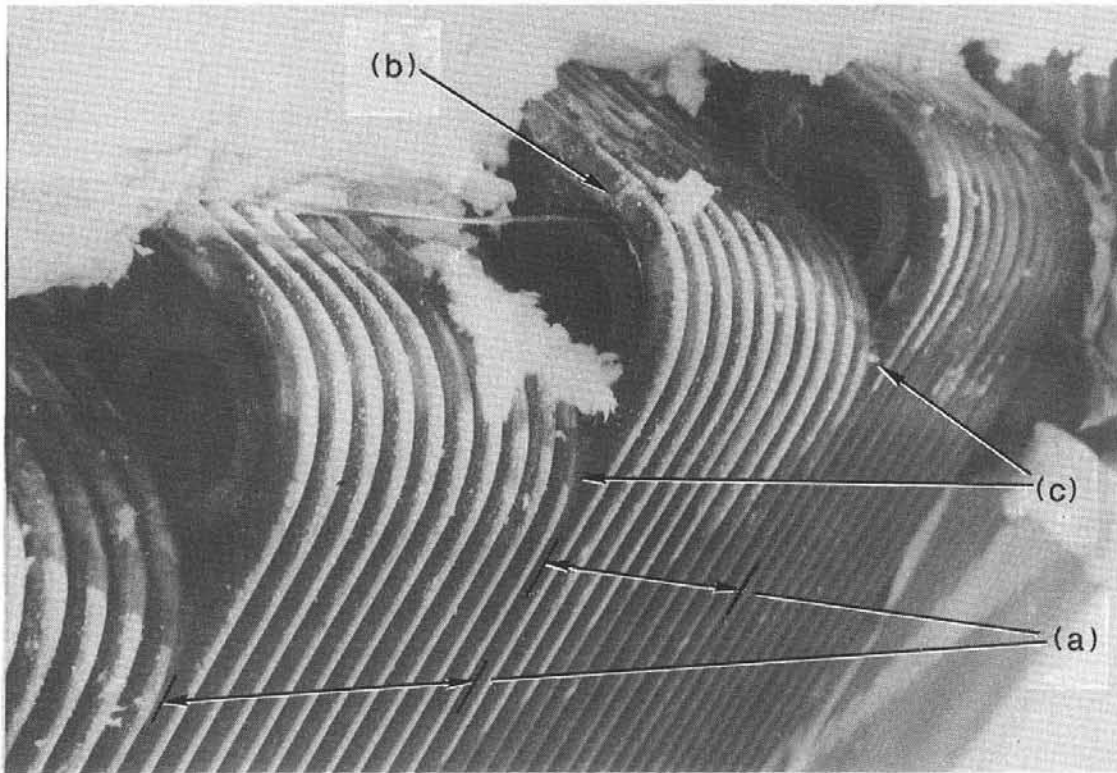
Figure 27. Photograph of the top portion of a panel, showing the subpanels (a), supports under the subpanel first 90° bend (b), and interstice welds on the front of the panel (c).

After the subpanels have been welded together, the inlet and outlet manifolds are welded to the tubes. The panel is then connected to the panel module support. Attachment brackets welded to the back of the panel, diagram (b) in Figure 26 at levels 1 through 6, are on each side of the panel, around tube 10 on one side and tube 60 on the other side. These brackets are connected to the panel module support with rollers, not shown in Figure 26. The rollers connected to the panel module and panel brackets are free to move as the panel changes temperature. Thus the panel, at levels 1 through 6, is free to move vertically on the panel module structure relative to level 7. These roller supports are designed to keep the panel from warping (radial deflection in and out along the panel normal) and bowing (decrease panel radius of curvature in the lateral or receiver circumferential direction). Level 7 (Figure 26), the top subpanel tube bend supports, is fixed and carries the panel weight. The panel module structure supports the panel weight, lateral (side to side), and radial (in and out) loads of the panel.

The first visible change we saw on the receiver was slight panel warpage in March 1982 after just two months of operation. A photograph of the receiver, Figure 28, shows the top portion of several receiver panels with areas of slight panel warpage identified. This warpage has no effect on receiver operation. Except for one panel, we believe this warpage is caused by lateral temperature gradients across the panel. Back surface metal temperature data at the top of each panel indicates that the north side of the panel is hotter than the south side. The hot side of the panel wants to expand more than the cool side of the panel. Since the tubes are welded together, the cool tubes restrain the expansion of the hot tubes and warpage occurs. The design of the panel supports and rollers may contribute to panel warpage by constraining the uneven panel growth. The exception is one panel which apparently overheated from loss of water flow. This panel expanded so much that it hit the bottom of the panel module support at level 1, Figure 26. To preclude this happening to other panels, we modified the module support on each boiler panel by extending its length to allow for more panel expansion. In 1982 we decided not to make any modifications to the panels to reduce the lateral temperature gradient or to the rollers to accommodate the uneven panel growth.

Since most of the heliostats in the heliostat field are north of the receiver, there is a lateral incident solar flux gradient across most of the panels. This flux gradient changes on the north panels as the sun moves from east to west. The tube orifice sizes on the east and west panels were selected to provide a flow distribution in these panels which would limit the lateral temperature gradient. Since the flux gradient changes on the north panels, these panels have uniform orifice sizes. To reduce the panel temperature gradient these tube orifices would need to be changed. The data which shows the panels have lateral temperature gradients also shows the panel north edge tube has the highest tube metal temperature. There are no orifices in the panel edge tubes. The space between adjacent panels allows the panel edge tubes to be exposed to incident radiation over about 270° around the tube while interior tubes are exposed over about 180°.

70
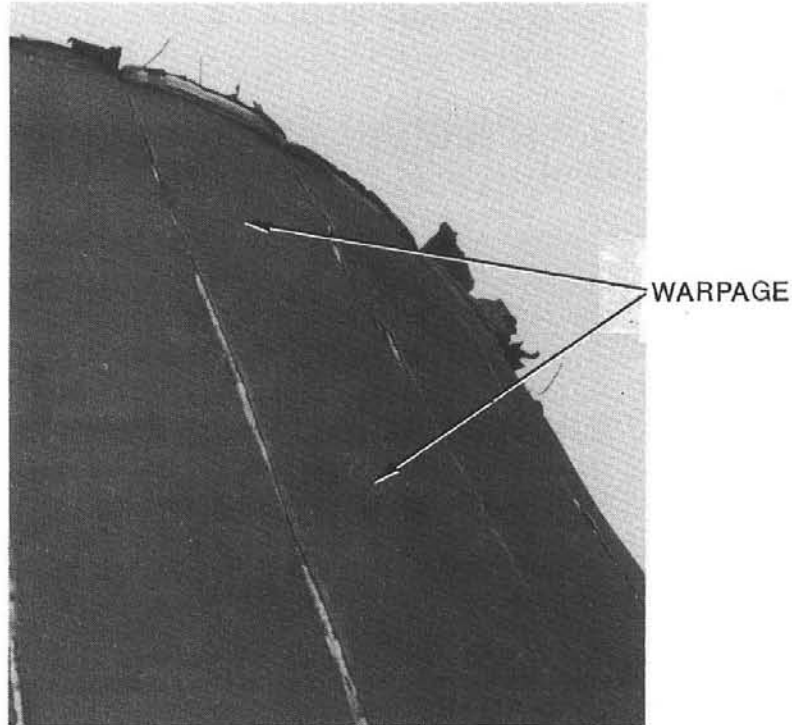
Figure 28. Photograph of the top portion of the receiver showing two panels with slight panel warpage.

After eighteen months of operation, July 1983, we found the first receiver tube leaks. These leaks occurred at the top, superheated section, of one panel on each side of the center subpanel at the interstice weld. In August 1983 we found a second type of tube leak. This new leak, on a different panel, was also at the top of the panel but on the panel north edge tube at the crown of the first 90° bend. This interstice weld and tube bend area of the panel is covered with insulation and is not exposed to the incident solar flux. Figure 29 shows a drawing of the top portion of a panel and the location of the leaks at the tube bend (a) and interstice weld (b). The subpanel tube bends are toward the inside (core side) of the receiver away from the incident solar radiation reflected from the heliostat field. The center subpanel interstice welds are between tubes 30/31 on one side and tubes 40/41 on the other side. These first interstice weld leaks are between tubes 30/31 and 40/41. Panel edge tubes are tubes 1 and 70. The portion of the panel not shown in Figure 29, tubes 51 through 70, is a mirror image of tubes 1 through 21. These leaks alone did not affect receiver operation but were the focus of an evaluation to find their cause and resulted in a plant shut down for their repair.

We performed several studies to determine the cause of these two types of leaks, interstice weld leak and tube bend leak, and a way to eliminate their occurrence. These studies were both analytical and experimental. Until we understood the cause of the leaks, we reduced the maximum receiver steam outlet temperature to about 410° C from the design value of 510° C. At first we hoped these

71
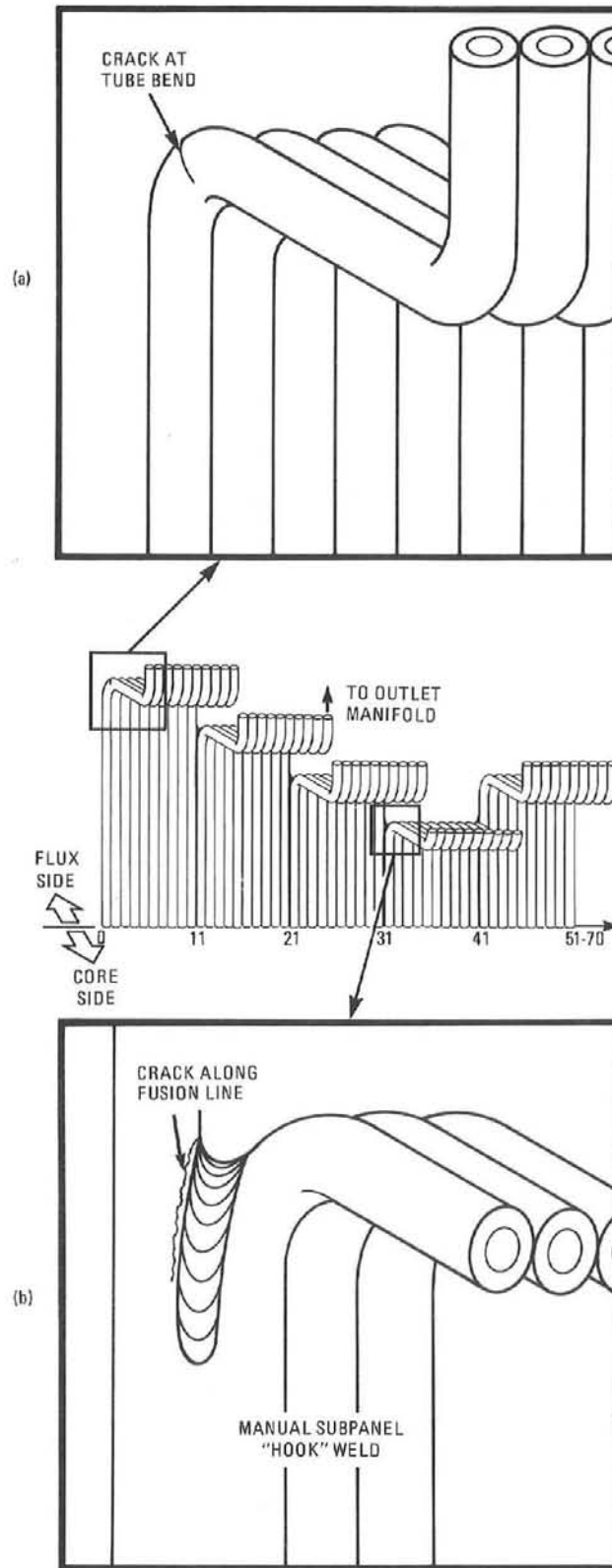
Figure 29. Drawing of the top portion of a panel showing the location of the leaks at the tube bend (a) and interstice weld (b). The tubes are bent toward the inside (core side) of the receiver away from the incident solar radiation.

leaks were exceptions and there was not a generic problem with the receiver. After several receiver inspections using dye penetrant and ultrasonics over a period of months, we found more interstice weld and tube bend cracks and leaks. This inspection data showed we had a tube leak problem affecting several receiver panels.

We removed a small section of the interstice weld and tube from the panel with this type of leak and replaced the section with new tube material in August 1983. Figure 30 is a photograph of the section of tube and weld removed from the panel with the interstice weld leak. Regions A and B show the termination of the crack next to the interstice weld. The crack is in the interstice weld fusion line between subpanels. The tube in Figure 30 is tube 30, from the subpanel next to the center subpanel. This tube is longer than the tubes in the center subpanel and extends beyond the interstice weld between tubes 30 and 31, see Figure 29. Region A in Figure 30 is on the front side of the panel and region B the back. We see in Figure 30 that the crack extended only a short distance toward the front of the panel compared to the back. Detailed fractography of the crack showed the crack initiated on the outside diameter of the tube near the weld heat affected zone and propagated into the tube. The crack surface striation spacing indicates the failure was due to low cycle fatigue.

In October 1983 we found another panel which had a leak at the interstice weld, next to the center subpanel, between tubes 30/31. By the end of 1983 the dye penetrant inspections of the interstice welds between each subpanel showed numerous cracks on several panels. A summary of our findings from inspecting the interstice welds is:

10 panels had cracks at one or more interstice welds

2 panels had leaks at one or more interstice welds
    adjacent to the center subpanel

The distribution of the cracks at the interstice welds showed that 70% occurred between tubes 30/31 and tubes 40/41. No cracks were found on the water preheat panels, panels 1-3 and 22-24.

Our analyses of the interstice weld area did not show conclusively the cause of this failure. The results showed that the magnitude of the stresses due to constraining the expansion, temperature increase, or contraction, temperature decrease, in the lateral direction were low compared to the material yield strength. This represents the case where the supports under each subpanel restrained the lateral subpanel movement. The highest stresses predicted in the interstice weld between subpanels occurred when there was a large temperature difference between adjacent subpanels. This condition could occur during receiver shut down if water at the saturation temperature flows to the top of one subpanel, which is still at the superheated steam temperature, before an adjacent subpanel. The
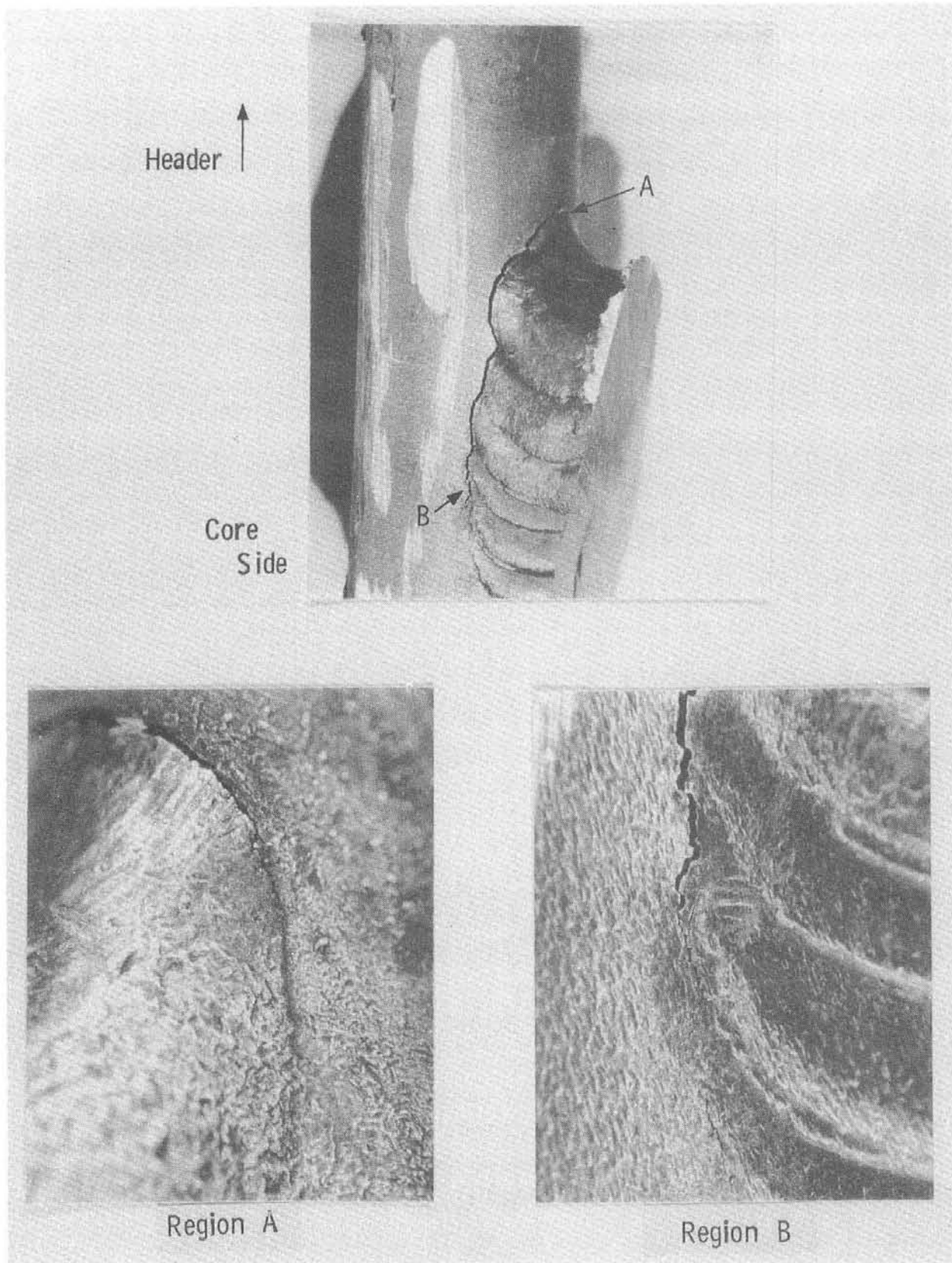
Figure 30. Photograph of the section of tube and weld removed from the panel with the interstice weld leak. Regions A and B show the termination of the crack next to the interstice weld.

data we evaluated from the tube metal temperatures at the top of a panel showed occurrences where a tube 35 temperature in the center subpanel would drop before tubes 5 and 65 temperature in the exterior subpanels. We did not have data for adjacent subpanels.

In January 1984 we decided to make modifications to all of the boiler panels to eliminate the occurrence of interstice weld cracks and leaks. While making the modifications we ground out all known cracks and weld filled those more than a 0.1 to 0.2 mm deep. We removed five of the seven supports under the subpanels, shown in Figure 27, at level 7 (Figure 26). We left supports under the two subpanels containing tubes 11-20 and tubes 51-60, Figure 28. We also ground away that portion on the interstice weld which extended to the front of the panel, Figure 27 (c), and a small portion on the back of the panel. At the interstice welds on each side of the center subpanels, we ground away the interstice weld for a length of about 100 mm down the panel. We tapered the termination of this grinding so that the weld was thin where the weld was removed and gradually thickened to its full thickness in about 25 mm. We believed that if these modifications did not reduce the stresses in the interstice region, then any crack which did occur would be in the tapered weld and not in the tube.

Since making these modification in January 1984, in addition to operation changes to be discussed, we have not had any interstice weld leaks. However, cracks are visible in the tapered region of some interstice welds adjacent to the center subpanels. This indicates the modifications did not relieve all of the loads in the interstice weld region of the panel.

At the same time we removed the cracked section of the interstice weld and tube; we removed the leaking edge tube bend and replaced it with a new tube bend (August 1983). The section of tube removed extended from below the first 90° tube bend, leak location, to above the second 90° tube bend, shown in Figure 29 (a). Figure 31 is a photograph of the crack in the edge tube bend section removed from a panel. We see in Figure 31 that the crack is circumferential in direction around the tube. The crack is located on the extrados, or outer curve, of the bend and wrapped around approximately 150° of the tube.

By November 1983 the ultrasonic inspections of the boiler panels first 90° tube bends showed that three panels had cracks in their edge tubes. One of these cracks was in the tube section we replaced in August 1983 when we removed the tube bend crack. In December 1983 we removed edge tube bends with cracks from two boiler panels and tube bends without cracks, material samples, from two other panels. The material samples were edge tubes from panels which we had data showing these edge tubes operated at lower temperatures than those which had cracked. A summary of the results of all of our ultrasonic inspections is:

9 panels had cracks or crack indication in their edge tubes

5 panels had leaks in their edge tubes

CIRCUMFERENTIAL
CRACK
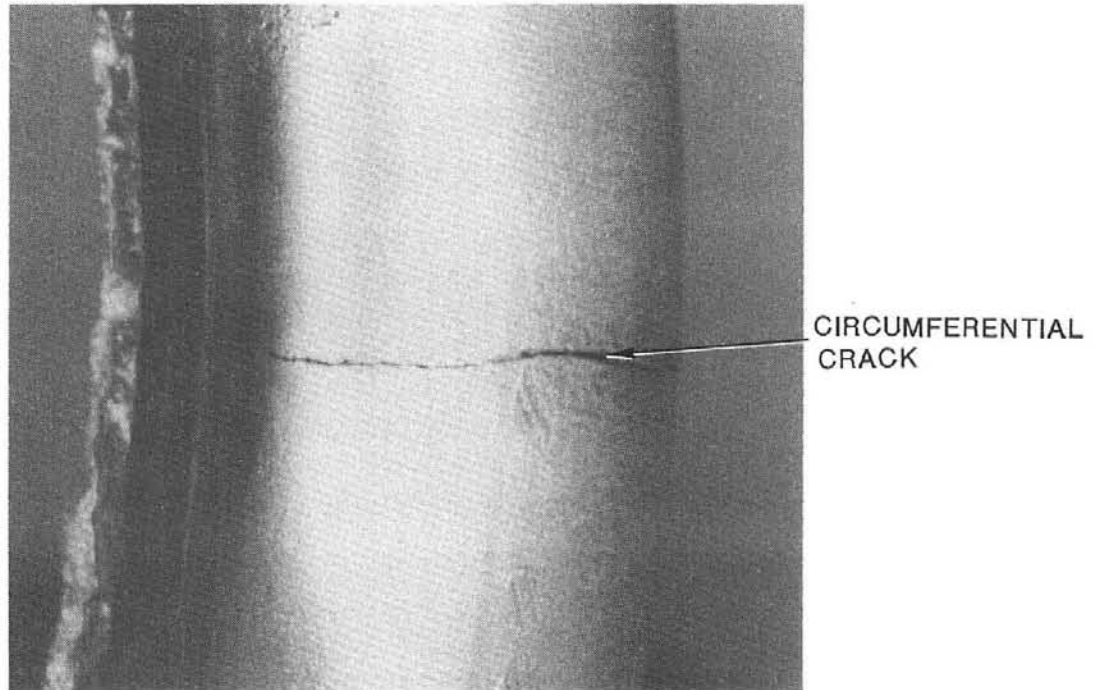
Figure 31. Photograph of the crack in the edge tube bend section removed from a panel. The crack is circumferential around the tube.

All of the cracks or leaks were in the north edge tubes which tend to operate at the highest temperature compared to other panel tubes. Also, the panel edge tubes with cracks had operated at higher temperatures than those panels without cracks.

We did a detailed metallographic evaluation on the tube bend sections removed from the panels. The results of this evaluation are reported in Reference 19. Also, the analyses on the interstice weld leaks were extended to cover the edge tube leaks. We found from our metallographic evaluation that these tube bend cracks initiated on the inside surface of the tube. Figure 32 is a photograph of the cross-section of one of the edge tube bends removed from a panel. We can see in Figure 32 the crack extended about 150° around the tube and the crack initiation site is on the tube extrados inside surface. Figure 33 is a low magnification photograph of the tube inside surface on the tube extrados, near the crack initiation site, from the tube shown in Figure 32. We can see in Figure 33 that there are many circumferential cracks, running perpendicular to the tube axis, and axial cracks, parallel to the tube axis. Further metallographic studies showed that the circumferential cracks are much deeper than the axial cracks. Several conclusions reported in Reference 19 are:

Cracks initiate on the inside diameter in the extrados of the tube bend;

76
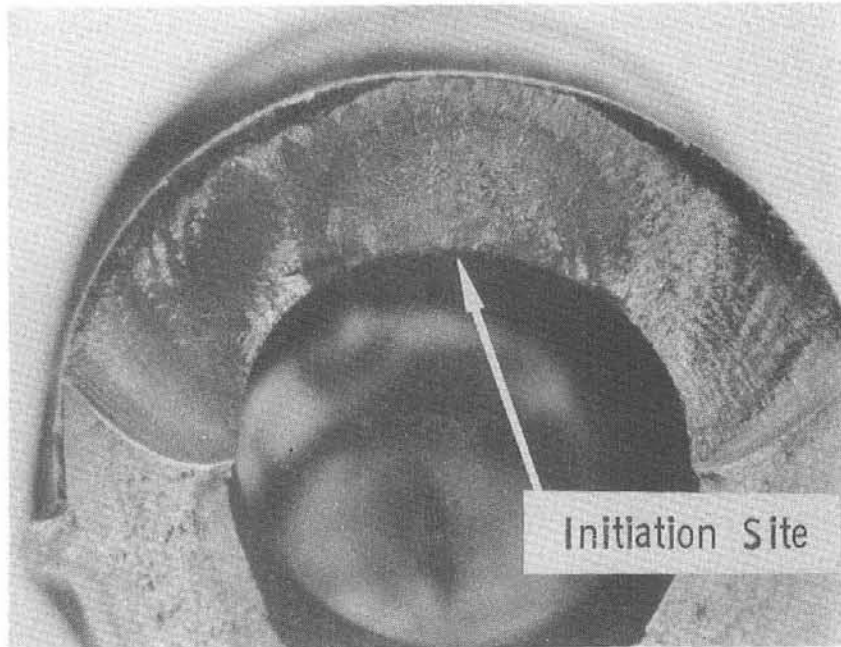
Figure 32. Photograph of the cross-section of one of the edge tube bends removed from a panel. The crack initiation site is on the tube inside surface.
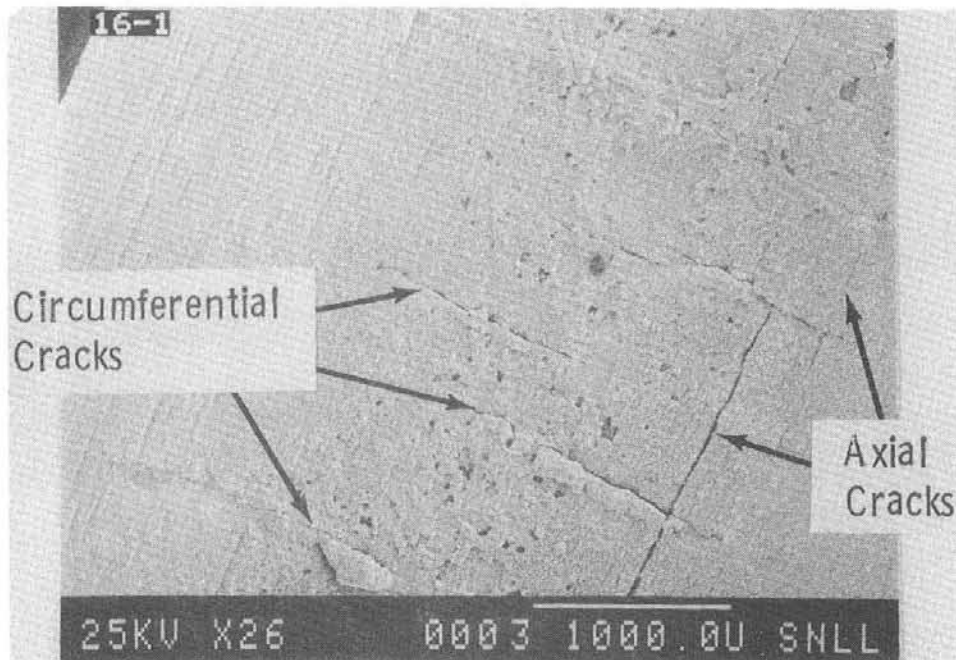
Figure 33. A low magnification photograph of the tube inside surface on the tube extrados, near the crack initiation site, from the tube shown in Figure 32. This surface has many circumferential and axial cracks.

Cracking occurs in both a circumferential and axial direction;

Cracking is transgranular for both types of cracks;

Only circumferential cracks propagated to the outside of the tube.

The two material samples from tubes which operated at lower temperatures did not have any cracks.

The appearance of the inside surface at the tube extrados indicates that the tube has experienced high circumferential and axial tensile stresses. These types of combined stresses could be caused if the inside surface of the tube were much cooler than the outside surface. This would be the case if during receiver shut down water at the saturation temperature impinged on the tube bend inside surface while it was still at the superheated steam temperature. This thermal shock would cause the cracks to initiate. Other types of loadings or repeated thermal shocks could then cause the crack to propagate through the tube wall.

The new tube section, installed in August 1983 to replace the first tube bend leak, showed an ultrasonic indication of a tube bend crack within six months of being replaced. This new tube section had a different mechanical environment than before since it was not welded to the adjacent tube. Yet, within six months it had cracked. The two material samples did not have inside surface cracks similar to those found in the other edge tube bend. However, these tube bend material samples had operated at lower temperatures than those where we found cracks. We believe thermal shock of the high temperature panel edge tubes is the cause of this type of cracks.

We were able to reproduce the type of cracking shown in Figure 33 in the laboratory. Tube samples were heated to high temperatures, about 650° C. Room temperature water was then injected into the tube at the extrados of the tube bend. The same types of cracks shown in Figure 33 were found on the tube inside surface.

To eliminate the occurrence of tube bend cracks on the receiver, we changed the operating procedure to reduce the outlet steam temperature to about 315° C, under controlled conditions, before receiver shut down. This controlled temperature decrease can be seen in Figure 22 at the end of the day and before the receiver shut down by removing heliostats from tracking the receiver. If water at the saturation temperature does impinge on the tube bend inside surface during receiver shut down, then the temperature difference between the inside and outside of the tube will be less than when cracks occurred. Also, to reduce the panels north edge tube temperatures, we installed radiation shields between the panels on over half the receiver. These radiation shields keep the incident radiation from impinging on the side of the edge tubes, which makes their radiation environment similar to interior panel tubes. At the time of these changes, there

were three panels which had edge tubes with known ultrasonic crack indications. Since these changes were made, all three tubes with known ultrasonic cracks indications have leaked. They were repaired by grinding out the cracks and filling it with weld material. However, no other edge tube bend leaks have occurred on the receiver.

In December 1983 while doing the interstice weld and tube bend inspections, we observed that more panels were becoming warped. Also, several panels were beginning to bow in the superheated portion. Bowing is a decrease in the panel radius of curvature in the lateral direction. We inspected the panel back surface support brackets and rollers and found that the bolts connecting the rollers to the panel module support were broken or bent. These bolt failures were found on nine panels with most at level 2 (Figure 26). As the panel temperature increases, the panels expand from the top, level 7, which is fixed. Thus, the bottom of the panels has the greatest vertical movement. If the rollers at level 2 bind and do not roll, then the panel will warp to accommodate the thermal expansion. An inspection of the rollers showed considerable corrosion and seizing of the rollers onto their axles. We modified the rollers in February 1984 to increase the tolerance between the roller and its axle.

After about forty-two months of receiver operation, July 1985, we found leaks on three panels at levels 5 and 6 where the attachment brackets are welded to the panel. Figure 34, a schematic of the attachment bracket, shows the location of the leaks. The "U" shaped clips in Figure 34 which are welded to the panel are 6.35 mm thick. The brackets are connected to these clips with pins. These clips are welded to tubes with a 2.93 mm wall thickness. The leaks are located at the ends of the clips near the weld boundary and are circumferential in direction. Similar leaks have been found on both sides of the panels. Since the first clip weld leaks in 1985, fifteen of the eighteen boiler panels have had clip weld leaks with most being at either level 5 or 6, or at both levels. Usually both sides of the panel at any given level have clip weld leaks. Repair of these clip weld leaks has been by the grind and weld fill method.

We originally thought these clip weld leaks were caused by the roller assembly binding and loading the clips. However, with the modification of the rollers to increase their tolerance, most rollers seem to roll freely. Also, the vertical movement of the panel at levels 5 and 6 is small compared to that at levels 1 and 2. We have not found any clip weld leaks at support levels 1 or 2. Another possible failure mode is that the supports at levels 1 through 6 are supposed to restrain the panels from bowing. With the panel front surface temperature higher than the back surface temperature, the panels will try to bow due to thermal expansion. This temperature difference is the greatest in the superheated portion of the panel. Constraining this bowing would load the clips. Figure 35 shows the predicted front surface temperature and incident flux density profile for a boiler panel (Figure 7), and the location of the panel support levels are shown as "∇'s". The support near 0 m panel length is level 1, and the support between 12 m and 14 m is level 7. We can see in Figure 35 that the level 6 support is in the panel
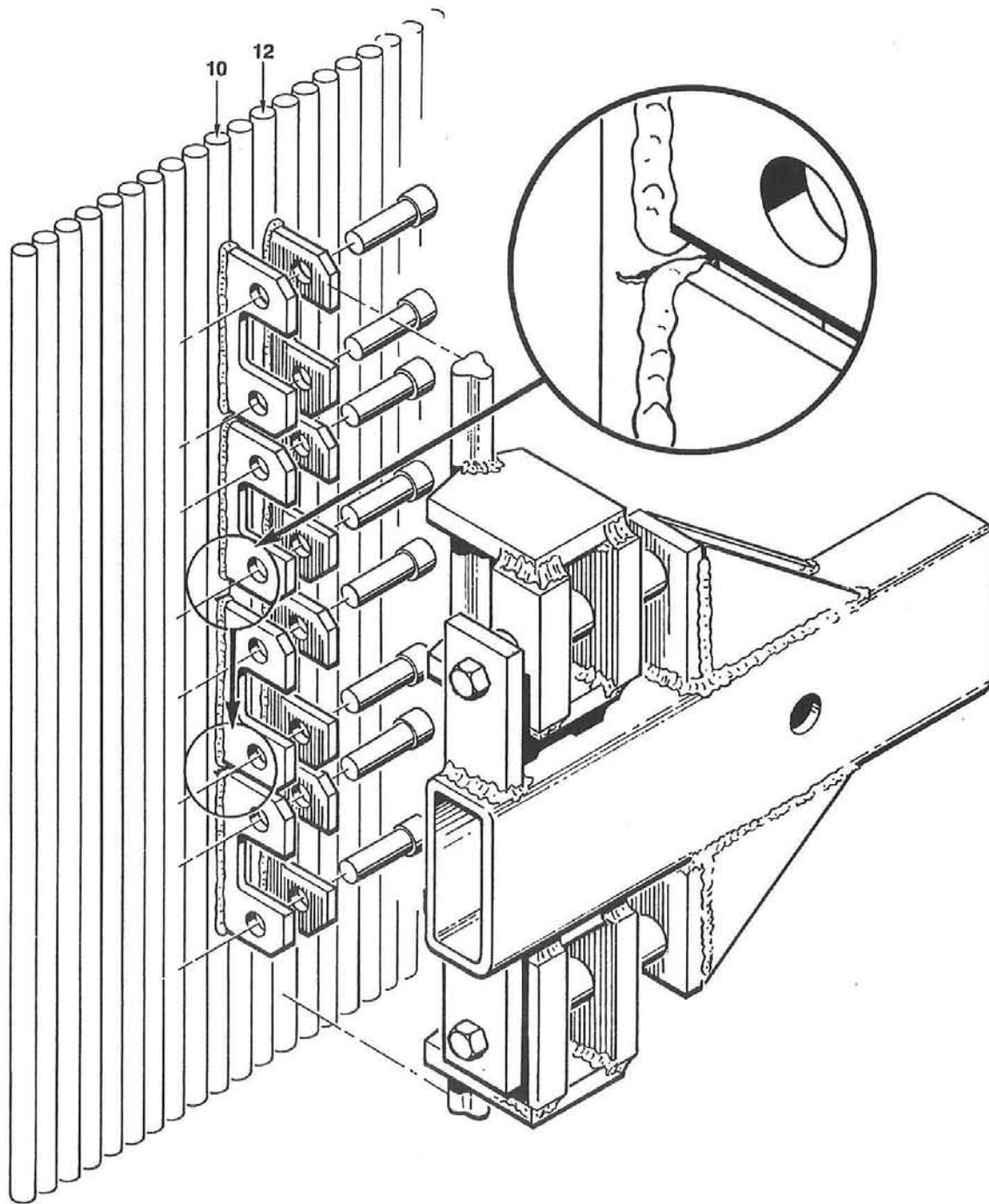
Figure 34. A schematic of the attachment bracket, showing the "U" shaped clips welded to the back of the panel. The leaks are located at the ends of the clips near the weld boundary and are circumferential in direction.

superheated steam portion, and the level 5 support is near the boundary of the saturated steam and superheated steam region.
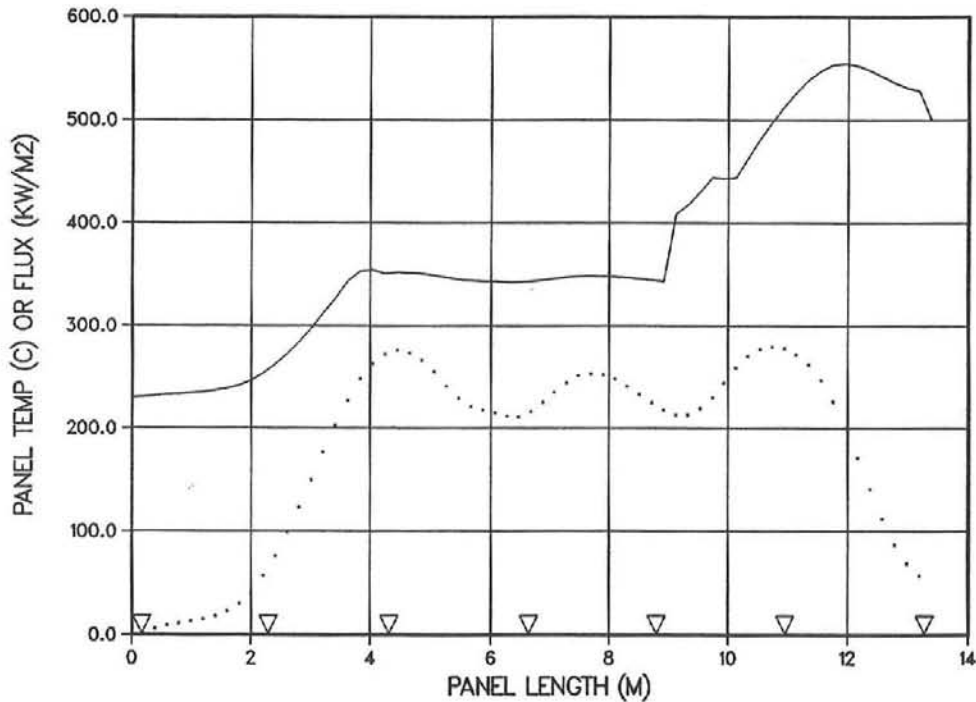
Figure 35. The predicted panel front surface temperature (solid line) and incident flux density (dash line) profiles for a boiler panel (Figure 7). The location of the panel support levels are shown as "▽'s" with level 1 support (Figure 26) near 0 m panel length.

Analyses of the clip stresses caused by the panel mechanical loads showed these stresses to be low compared to the material yield strength. These analyses also showed that the support at level 6 could be removed without a large increase in the clip stresses at level 5. The analyses did show that the thermal stress between the panel tube and clip, due to the temperature gradient normal to the panel in the clip, would result in high stresses. These stresses are highest in the high temperature portion of the panel.

We believe that the clip weld leaks are caused, among other factors, by thermal stresses in the weld region due to the temperature gradient between panel tube/clip weld and the clip material away from the tube. We modified the boiler panels by removing the supports and clips at level 6. We also modified the support and clips on two panels at level 5, but this modification did not work. The modification on these two panels removed all but a portion of two sets of clips and restrained the panel radial movement with cables. Removing the clips reduced the clip weld leaks; however, the cable supports did not restrain the panel radial movement. We continued to have clip weld leaks with some now occurring at level 4. As long as we have these types of clips welded to the panel, there is a chance we will have clip weld leaks.

81

In June 1986 one panel north edge tube had a leak on the front side of the tube about 4 m below the top tube bend. We inspected this tube and found many circumferential cracks from 0.5 m above the leak to over 1 m below the leak. The appearance of the surface of this tube indicates that it has experienced very high temperatures. Tube back surface metal temperatures at the top of the panel shows that this edge tube has operated at higher temperatures than any other panel edge tube. We were told by people who have extensive experience in superheated boilers that this type of crack is called "fire cracking" and occurs in superheated boilers when the tube has operated at high temperatures. We repaired this leak by replacing a 6 m section of the tube from above the top first 90° tube bend. As of the end of 1987, only one other panel edge tube has had a fire cracking failure.

The best engineering practices at the time were used to design the Solar One receiver panels to have a 30-year life. Within eighteen months of the start of receiver operation, leaks began to occur in panel tubes. As receiver operation continued, we found new and different types of tube leaks. Table X summarizes the types of tube leaks and when they first occurred. Time of occurrence is in months from the start of receiver operation when a particular type of leak was first found and the type is by location on the panel. For each type of leak or leak location we evaluated the cause of the failure and possible solutions. We made modifications to the receiver panels or to the operation procedures to eliminate the occurrence of the various types of leaks. We were successful in eliminating the interstice weld and north edge tube bend leaks, but clip weld leaks are still occurring. Since only two north edge tubes have had front surface fire cracking leaks, we did not make panel modifications to eliminate this type of leak. The radiation shields we installed between the panels to reduce the operating temperature of the north edge tubes should have a positive effect of limiting the front surface tube leaks. By reducing the maximum steam outlet temperature to below 450°C, we hope the frequency of occurrence of the clip weld leaks is reduced.

TABLE X

SUMMARY OF THE RECEIVER TUBE LEAKS

Time of occurrence (months)	Leak location
18	interstice weld next to the center subpanel
19	north edge tube at the top 90° bend
42	panel back surface clip weld
53	north edge tube front surface below tube bend

The severity of the panel warpage and bowing has increased with time. Modifications to the panel roller supports to allow the supports to move freely on the panel module support have not eliminated the warpage and bowing deformations.

Figure 36, a recent photograph of the top portion of the receivers, shows how severe these deformations are compared to the earlier photograph in Figure 28. We can see in Figure 36 the radiation shields we installed between most of the panels on the receiver. Panel warpage and bowing does not affect receiver operation other than exposing the panel supports behind the panel to incident solar radiation. However, such deformations must be reducing the receiver life and most likely will lead to additional tube leaks on the receiver. We have installed additional insulation to protect the panel supports.
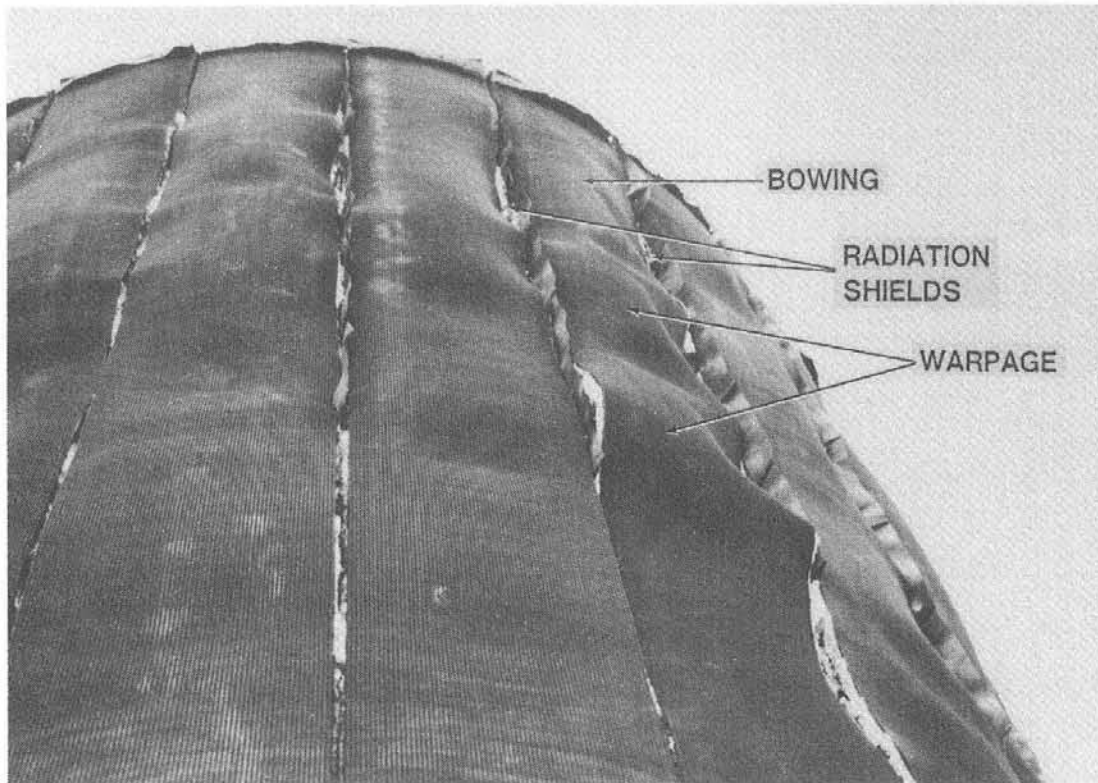
Figure 36. Photograph of the top portion of the receivers, showing the current panel warpage and bowing. The radiation shields installed between the panels protect the sides of the edge tubes from incident radiation.

After more than seventy months of receiver operation we have learned many things about receiver life. Most tube leaks have been associated with some type of weld on the panels. We need to reduce the number of welds and be concerned with the relative size of materials welded to the tubes. Over-constraining the panel thermal expansion can lead to high thermal stresses in the panel tubes. The severe thermal environment and exposure to weather can cause corrosion on the panel supports and restrict their movement. Temperature gradients due to lateral incident solar flux gradients and panel front to back surface temperatures during start-up, cloud transients, and shut-down can cause thermal creep-fatigue leading to panel warpage and bowing. Having the panel tubes welded together along their length when the panel has a lateral temperature gradient can lead to

panel deformation. The designers of the next generation of receivers will need to learn from what we have experienced at Solar One.

Conclusions

We used experimental data to evaluate the performance of the Solar One receiver. The receiver performance characteristics included point-in-time steady state efficiency, average efficiency, receiver life, start-up time, operation time, and operations during cloud transients. Each performance characteristic was studied using experimental data from the five years of receiver operation.

We found that our results for the peak receiver point-in-time efficiency, before the receiver was repainted and using Equation (1), were 76.7% ± 4%, nearly the same as earlier reported in References 4 and 5. We used a different method to calculate the receiver point-in-time efficiency, independent of the receiver incident power. We found that this different method gave a receiver efficiency of 76.1% ± 2.6% at a slightly lower value of the receiver absorbed power than the peak using the incident power. We compared the results from both methods of calculating the receiver efficiency with the design predictions. The two results using experimental data gave nearly the same efficiency at the same value of the receiver absorbed power and both were lower than the design prediction. We found the difference between the experimental results and prediction could be accounted for, in part, by the receiver surface solar absorptance.

After the receiver was repainted in December 1985, we calculated the peak receiver point-in-time efficiency from experimental data and found the efficiency to be about 81%. This value, after repainting the receiver, was nearly the same as the design prediction for slightly different receiver operating conditions. Receiver thermal losses, calculated by two different techniques using experimental data, were the of the same order of magnitude as those from the design predictions. This comparison between experimental and design results shows, for the Solar One water/steam external receiver, that predictions of the receiver efficiency and thermal losses were realistic.

We found that the average receiver efficiency was within 5 to 10 percentage points of the peak point-in-time receiver efficiency. This average was for receiver operations with receiver start-up in about 1.6 hours after sunrise and shut-down near sunset. We showed that receiver start-up times could be reduced by using a different heliostat aimpoint strategy. We also found the receiver could operate through certain types of cloud transients, which affects the average receiver efficiency, if there was a slight delay between extreme changes in the site insolation. However, severe receiver front surface temperature ramp rates, during operation in cloud transients and start-up, may affect receiver life.

The nearly continuous operation of the Solar One receiver, from sunrise to sunset, for over five years gave us the first real opportunity to evaluate receiver

life. We found as the time of receiver operation increased, different types of receiver tube leaks and panel failures occurred. We modified the receiver panels and changed the receiver operation procedures to try to eliminate some of the tube leaks and panel failures. Further receiver operation showed the modifications were successful in some cases and not in others. Without a major re-design and modification to the receiver panel supports, we will not be able to eliminate all the problems affecting receiver life.

We have shown that our methodology for predicting receiver point-in-time efficiency and thermal losses gave reasonable results when compared to experimental data. However, improvement should be made in both the experimental and analytical techniques of evaluating these parameters.

We believe it is unlikely that the Solar One receiver will have a 30-year life. Receiver life which is affected by receiver start-up, cloud transients, receiver shutdown, and panel supports is an area which requires further evaluation.

APPENDIX A

THERMAL LOSS TEST EVALUATION

To evaluate the receiver thermal loss and part-load performance for the receiver thermal loss tests which were performed at Solar One, we used the following assumptions and equations:

Part-Load Performance

The receiver efficiency is defined as the receiver absorbed power (ABS), calculated from measured temperatures and flow, divided by the receiver incident power (INC), predicted using measured data and a heliostat field performance value

$$\text{Receiver efficiency} = \frac{\text{ABS}}{\text{INC}} \qquad (A-1)$$

The receiver incident power can be expressed as

$$\text{INC} = \text{I} \times \text{REF} \times \text{NT} \times \text{NF} \times \text{A} \qquad (A-2)$$

where,

I	=	measured direct normal insolation
REF	=	measured heliostat mirror reflectivity
NT	=	number of heliostats tracking the receiver
NF	=	heliostat field performance value
A	=	area of an individual heliostat

The heliostat field performance value (NF) can be thought of as being the product of several factors related to the heliostat field, site, and time of day. For example,

NF_{cosine}	=	sun's position relative to the heliostat
NF_{shadow}	=	one heliostat shadows the sun from another
NF_{block}	=	one heliostat blocks the reflected beam of another
NF_{tower}	=	tower shadows some heliostats
$\text{NF}_{atm\ attn}$	=	atmospheric attenuation of the reflected beam
$\text{NF}_{sunshape}$	=	effect of sunshape on the reflected beam
NF_{error}	=	effect of heliostat errors on the reflected beam

the first four factors listed are a function of the time of day and the heliostat, tower, and heliostat field geometry. All of these factors can be calculated with

accuracy for a given time and heliostat field. The next two factors are a function of the atmosphere at the site and the last on the heliostat tracking, pointing, and mirror errors. In general, we know less about the last three factors, but within the hour or so it takes to run the thermal loss test, we assume the atmosphere does not change nor do the heliostat errors. Most heliostat performance codes include the effect all of these factors when calculating the incident power on the receiver, but there are always questions about how well we know the input to the codes for the last three factors listed. For this analysis, the important thing is that whatever effects the last three factors have, they do not change within the time it takes to do the thermal loss tests.

The receiver part-load (p) efficiency - as a fraction of the receiver full power (f) efficiency - can be determined from the following equation

$$\text{Part} - \text{load fraction} = \frac{\text{ABS}_\text{p}/\text{INC}_\text{p}}{\text{ABS}_\text{f}/\text{INC}_\text{f}} \qquad (A-3)$$

Using Equation (A-2) in Equation (A-3) and rearranging gives

$$\text{Part} - \text{load fraction} = \frac{(\text{I}_\text{f} \times \text{REF} \times \text{NT}_\text{f} \times \text{NF}_\text{f} \times \text{A}) \times \text{ABS}_\text{p}}{(\text{I}_\text{p} \times \text{REF} \times \text{NT}_\text{p} \times \text{NF}_\text{p} \times \text{A}) \times \text{ABS}_\text{f}} \qquad (A-4)$$

For the tests on the same day, we assumed that the mirror reflectivity (REF) did not change during the day. We know the heliostat area (A) is constant. Equation (A-4) reduces to

$$\text{Part} - \text{load fraction} = \frac{(\text{I}_\text{f} \times \text{NT}_\text{f} \times \text{NF}_\text{f}) \times \text{ABS}_\text{p}}{(\text{I}_\text{p} \times \text{NT}_\text{p} \times \text{NF}_\text{p}) \times \text{ABS}_\text{f}} \qquad (A-5)$$

When tests are run near solar noon, it might be assumed the heliostat field performance value is constant. This assumption can be checked by calculating the ratio of $\text{NF}_\text{f}/\text{NF}_\text{p}$ to see if it is equal to or very near unity. It is the ratio of $\text{NF}_\text{f}/\text{NF}_\text{p}$ which is important and not their absolute values. If the same parameters for the site atmosphere, sunshape, and heliostat errors are used, then only those factors affected by the time of day would change. We believe we can predict the effect of the change in the time of day on NF. This could be important if the tests were run over several hours rather than near solar noon. If the assumption of a constant heliostat field performance value is true, then Equation (A-5) can be evaluated using only measured data. Note, bias errors could cancel out leaving only random errors affecting the results.

Thermal Loss Predictions

It is assumed that the receiver absorbed power can be expressed as a linear relationship to the receiver incident power and thermal loss (L) as follows

$$ABS = NA \times INC - L \qquad (A-6)$$

where NA is an effective receiver solar absorptance. Let (1) be a part power test, (2) the full power test, and (3) the complementary part power test of (1). Thus, for the three power levels Equation (A-6) can be written, using Equation (A-2) as

$$ABS_1 = NA \times I_1 \times REF \times NT_1 \times NF_1 \times A - L_1 \qquad (A-7)$$

$$ABS_2 = NA \times I_2 \times REF \times NT_2 \times NF_2 \times A - L_2 \qquad (A-8)$$

$$ABS_3 = NA \times I_3 \times REF \times NT_3 \times NF_3 \times A - L_3 \qquad (A-9)$$

We define the following ratios

$$IR1 = \frac{I_2 \times NF_2}{I_1 \times NF_1} \qquad (A-10)$$

$$IR3 = \frac{I_2 \times NF_2}{I_3 \times NF_3} \qquad (A-11)$$

When we evaluate Equations (A-10) and (A-11), we recall that if the thermal loss test is performed near solar noon, then it might be that $NF_1 = NF_2 = NF_3$. If not, then again the ratios of NF_2/NF_1 and NF_2/NF_3 would need to be calculated. We multiply Equation (A-7) by Equation (A-10) and Equation (A-9) by Equation (A-11). We add the resulting equations and subtract the result from Equation (A-8) which gives, after rearranging,

$$
\begin{aligned}
ABS_2 - (IR1 \times ABS_1 + IR3 \times ABS_3) = \\
I_2 \times NF_2 \times REF \times NA \times (NT_2 \times A - (NT_1 \times A + NT_3 \times A)) - \\
L_2 + (IR1 \times L_1 + IR3 \times L_3)
\end{aligned}
\qquad (A-12)
$$

By definition of the test method

$$NT_2 \times A = NT_1 \times A + NT_3 \times A \qquad (A-13)$$

thus, the first term after the equal sign in Equation (12), using Equation (A-13), is zero. We define two additional ratios as

$$LR1 = \frac{L_1}{L_2} \qquad (A-14)$$

$$LR3 = \frac{L_3}{L_2} \qquad (A-15)$$

and substituting Equations (A-14) and (A-15) into Equation (A-12), after factoring L_2 from the last term, results in

$$ABS_2 - (IR1 \times ABS_1 + IR3 \times ABS_3) = L_2 \times (IR1 \times LR1 + IR3 \times LR3 - 1) \quad (A-16)$$

Solving Equation (A-16) for L_2 gives

$$L_2 = \frac{ABS_2 - (IR1 \times ABS_1 + IR3 \times ABS_3)}{IR1 \times LR1 + IR3 \times LR3 - 1} \qquad (A-17)$$

This is the equation for the total thermal loss from the receiver at the full power test level. It is independent of knowing the absolute value of the receiver incident power. To solve this equation, an estimate of the thermal loss at each test level needs to be made, i.e., estimates of LR1 and LR3. Needing these estimates of LR1 and LR3 to solve Equation (A-17) is a deviation from using only measured data to determine the receiver thermal loss. We will show how we used the measured receiver absorbed power and receiver geometrical data to make our estimates of LR1 and LR3.

If it is assumed that the thermal loss tests are run near solar noon, i.e., NF is constant, the insolation is constant during the tests, and the loss is the same at each power level, then the Equation (A-17) would reduce to

$$L_2 = ABS_2 - (ABS_1 + ABS_3) \qquad (A-18)$$

This equation will give a minimum value for L_2, since in general LR1 and LR3 are less than unity.

90

Once the receiver thermal loss has been calculated using Equation (A-17), since it is not assumed the insolation and thermal losses are constant, then the receiver full power efficiency is calculated by

$$\text{Efficiency} = \frac{\text{effective solar absorptance}}{1 + L_2/ABS_2} \qquad (A-19)$$

This equation is derived by solving Equation (6) for INC, substituting the results into Equation (1), and rearranging. Equation (A-19) is independent of the receiver incident solar power. The effective solar absorptance in Equation (A-19) accounts for the receiver heat exchanger active surface solar absorptance, tube geometry, and the difference between the active area and that exposed to the incident solar power; for example, gaps between the receiver panels.

Thermal Loss Predictions (Receiver Model)

Equations (A-14) and (A-15) require an estimate be made for the receiver thermal loss at each test power level. These two equations are used in Equation (A-17) to find the full power test level thermal loss. To make this estimate, a receiver thermal loss model is developed which uses measured data from the thermal loss tests.

To estimate the receiver emitted radiation loss, each receiver panel is treated separately. Preheat panels (1, 2, 3, 22, 23, and 24) are treated as whole panels, and the boiler panels (4-21) are treated in three equal sections, i.e. water, boiling, and steam. Convection loss is calculated for the entire receiver. Conduction loss is assumed negligible and not included. The receiver predicted thermal loss at each power level is the sum of the individual panel emitted radiation losses and receiver convection loss. Data from the test at each power level on data tapes is used to calculate each panel, panel section, and the receiver absorbed power. Data used included panel and receiver inlet water and outlet steam temperatures, pressures, mass flow, air temperature, and wind speed. Based on the inlet and outlet temperatures and pressures and mass flow, we calculate the absorbed power for each panel or boiler panel section and the entire receiver.

To predict the individual panel emitted radiation and receiver convection loss an estimate of the panels and receiver average surface temperatures is calculated. The approach used followed the method given in Reference 18 for concentric cylinders with fluid flowing inside. For a panel each tube consists of a layer of high solar absorptance paint, the steel tube, and the fluid inside the tube. In the steady state, the heat flow through each portion of the tube is the same and is represented by

$$\text{ABS}_t = h_{\text{fluid}} \times A_{\text{is}} \times (T_{\text{is}} - T_{\text{fluid}}) \quad \text{for the inner surface} \qquad (A-20)$$

$$\text{ABS}_t = k_{\text{st}} \times A_{\text{st}} \times \frac{(T_{\text{os}} - T_{\text{is}})}{(r_{\text{os}} - r_{\text{is}})} \quad \text{for the steel tube} \qquad (A-21)$$

$$\text{ABS}_t = k_p \times A_p \times \frac{(T_{\text{wall}} - T_{\text{os}})}{(r_{\text{op}} - r_{\text{os}})} \quad \text{for the absorptance paint} \quad (A-22)$$

where we assume that the heat transfer occurs only through the top half of the tube exposed to the solar flux and

ABS_t = calculated heat absorbed by an individual panel tube (preheat panels) or panel section tube (boiler panels)
$\text{ABS}_t = m \times (h_{\text{out}} - h_{\text{in}}) \quad \text{MW}_t$

m = tube mass flow, kg/sec

h_{out} = fluid enthalpy at T_{out}, kj/kg

h_{in} = fluid enthalpy at T_{in}, kj/kg

h_{fluid} = fluid film coefficient for either water, boiling water, or superheated steam, $\text{MW}_t/\text{m}^2 -^\circ \text{C}$

r_{is} = steel tube inside radius, 0.00342 m

ℓ_p = tube active length (preheat panel), 13.7 m

ℓ_s = tube active length (boiler panel sections), 4.57 m

A_{is} = half of the preheat panel tube inside surface area
$A_{\text{is}} = \pi \times r_{\text{is}} \times \ell_p \quad \text{m}^2$
or for a boiler panel section
$A_{\text{is}} = \pi \times r_{\text{is}} \times \ell_s \quad \text{m}^2$

T_{is} = steel tube inside surface temperature, $^\circ$C
T_{fluid} = mean fluid temperature

$T_{\text{fluid}} = (T_{\text{inlet}} + T_{\text{outlet}})/2 \quad ^\circ$C

k_{st} = steel thermal conductivity, $17.3 \times 10^{-6} \quad \text{MW}_t/\text{m} -^\circ \text{C}$ at 400°C

A_{st} = logarithmic mean area of half the preheat panel steel tube,
$A_{\text{st}} = (\pi \times \ell_p \times (r_{\text{os}} - r_{\text{is}}))/(\ln(r_{\text{os}}/r_{\text{is}})) \quad \text{m}^2$
or for a boiler panel section
$A_{\text{st}} = (\pi \times \ell_s \times (r_{\text{os}} - r_{\text{is}}))/(\ln(r_{\text{os}}/r_{\text{is}})) \quad \text{m}^2$

T_{os} = steel tube outside surface temperature, °C

r_{os} = steel tube outside radius, 0.00635 m

k_p = absorptance paint thermal conductivity, $0.6 \times 10^{-6} \quad \text{MW}_t/\text{m} -^\circ \text{C}$

A_p =   logarithmic mean area of half the preheat panel paint surface,
$A_p = (\pi \times \ell_p \times (r_{op} - r_{os}))/(\ln(r_{op}/r_{os}))$ m^2
or for a boiler panel section
$A_p = (\pi \times \ell_s \times (r_{op} - r_{os}))/(\ln(r_{op}/r_{os}))$ m^2

T_{wall} =   front surface temperature of the absorptance paint, °C

r_{op} =   outside surface radius of the absorptance paint
assuming a paint thickness of 45 μm, 0.006395 m

Fluid properties are evaluated at T_{fluid}. Using Equations (A-20), (A-21), (A-22), and the definition of T_{fluid} the average preheat panel tube front surface temperature or average boiler panel tube section front surface temperature (T_{wall}) can be found from

$$T_{wall} = (T_{inlet} + T_{outlet})/2 + \frac{ABS_t}{h_{fluid} \times A_{is}}$$

$$+ \frac{ABS_t \times (r_{os} - r_{is})}{k_{st} \times A_{st}} + \frac{ABS_t \times (r_{op} - r_{os})}{k_p \times A_p} \qquad (A-23)$$

We assume that the fluid inlet and outlet temperatures for a tube within a preheat panel is the same as that for the panel. For the boiler panels we assume that the fluid inlet temperature of the subcooled section is the same for all boiler panels. The outlet temperature of the subcooled section is the water saturation temperature at the mean boiler panel pressure. The inlet and outlet temperature of the boiling section of the boiler panels is the saturation temperature, but the inlet enthalpy is that of saturated water and the outlet enthalpy is that of saturated steam. The inlet temperature of the superheat section of the boiler panels is the saturation temperature, and the outlet temperature is the panel outlet temperature. Since there are 70 tubes per panel, and if it is further assumed that the flow in each tube within a panel is equal, then

mass flow per tube = (panel mass flow)/70

Thus, by knowing a panel or panel section fluid inlet and outlet temperature and pressure and the panel mass flow, an estimate of each panel or panel section average front surface temperature can be made using Equation (A-23). The receiver average surface temperature is calculated by using the average of the twenty-four panel average surface temperatures. Since Equation (A-23) is dependent on the panel absorbed power, the panel and receiver average surface temperatures will increase as the absorbed power increases even though the receiver inlet and outlet temperatures are constant during each test power level.

Both natural and forced convection heat transfer correlations used are those from Siebers (Ref 16,) and they were increased to account for the tube geometry of the receiver. A mixed convection heat transfer coefficient is found using

the natural and forced convection heat transfer coefficients as recommended by Siebers.

The prediction of the receiver thermal loss at each power level for the thermal loss tests used the following definitions and values

σ	=	Stefan-Boltzmann constant, 5.669×10^{-8} w/m^2 $-^\circ$ K^4
dia	=	receiver diameter, 7.01 m
g	=	acceleration of gravity, 9.8 m/sec^2
ϵ	=	panel effective emittance, .90
A_{panel}	=	panel projected area, 12.09 m^2
$A_{section}$	=	panel section projected area, 4.03 m^2
V	=	wind speed, m/sec
T_∞	=	ambient air temperature, $^\circ$K
ν	=	air kinematic viscosity, m^2/sec
β	=	air temperature coefficient of volume expansion, 1/$^\circ$K
k_{air}	=	air thermal conductivity, w/m $-^\circ$ K
Pr_{air}	=	air Prandtl number
T_{wall_s}	=	panel section average front wall temperature (boiler panels), (A-23) $^\circ$K
T_{wall_p}	=	panel average front wall temperature (preheat panels), (A-23) $^\circ$K

$$T_{wall_p} = \frac{\sum_{n=1}^{3} (T_{wall_s})_n}{n} \ \ ^\circ K \text{ (boiler panels)}$$

T_{wall_R}	=	receiver average front wall temperature

$$T_{wall_R} = \frac{\sum_{n=1}^{24} (T_{wall_p})_n}{n} \ \ ^\circ K$$

Re_{air}	=	receiver Reynolds number

$$Re_{air} = \frac{V \times dia}{\nu}$$

Gr	=	receiver Grashof number

$$Gr = \frac{g \times \beta \times \ell_p^3 \times (T_{wall_R} - T\infty)}{\nu^2}$$

Nu_{nat}	=	receiver natural convection Nusselt number

$$Nu_{nat} = .404 \times (Gr^{\frac{1}{4}}) \times (\frac{T_{wall_R}}{T_\infty})^{-0.04} \text{ for Gr} < 1.0 \times 10^9$$

$$Nu_{nat} = .098 \times (Gr^{\frac{1}{3}}) \times (\frac{T_{wall_R}}{T_\infty})^{-0.14} \text{ for Gr} \geq 1.0 \times 10^9$$

$H_{natural}$	=	receiver natural convection heat transfer coefficient

$$H_{natural} = \frac{\pi}{2} \times \frac{Nu_{nat} \times k_{air}}{\ell} \ \ \text{w/m}^2 -^\circ \text{ K}$$

Nu_{for}	=	receiver forced convection Nusselt number

$$Nu_{for} = .453 \times (Re^{\frac{1}{2}}) \times (Pr_{air}^{\frac{1}{3}}) \text{ for Re} < 2.0 \times 10^5$$

$$Nu_{for} = .0307 \times (Re^{0.8}) \times (Pr_{air}^{0.6}) \times (\frac{T_{wall_R}}{T_\infty})^{-0.4} \text{ for Re} \geq 2.0 \times 10^5$$

94

H_{forced} = receiver forced convection heat transfer coefficient

$$H_{forced} = \frac{\pi}{2} \times \frac{Nu_{for} \times k_{air}}{dia} \quad \text{w/m}^2 - ^\circ\text{K}$$

H_{mix} = mixed air convection heat transfer coefficient

$$H_{mix} = (H_{forced}^{3.2} + H_{natural}^{3.2})^{\frac{1}{3.2}} \quad \text{w/m}^2 - ^\circ\text{K}$$

where air properties are evaluated at ambient temperature.

Each preheat panel emitted radiation loss (L_r) is then

$$L_r = \epsilon \times \sigma \times A_{panel} \times [T_{wall_p}{}^4 - T_\infty{}^4] \qquad (A-24)$$

and each boiler panel emitted radiation loss is

$$L_r = \sum_{n=1}^{3} \epsilon \times \sigma \times A_{section} \times [(T_{wall_s})_n{}^4 - T_\infty{}^4] \qquad (A-25)$$

and the receiver emitted radiation loss (L_R) is then

$$L_R = \sum_{n=1}^{24} (L_r)_n \qquad (A-26)$$

the receiver convection loss (L_C) is

$$L_C = 24 \times A_{panel} \times H_{mix} \times (T_{wall_R} - T_\infty) \qquad (A-27)$$

and the total receiver predicted thermal loss is

$$L_{total} = L_R + L_C \qquad (A-28)$$

Based on the surface temperatures calculated using equation (A-23) the receiver emitted radiation loss (A-26), mixed convection loss (A-27), and total loss (A-28) is calculated for each of the three power levels during the thermal loss test. These results are used in equations (A-14) and (A-15). Equation (A-17) is used to calculate the receiver thermal loss at the full power condition and Equation (A-19) the efficiency. Equation (A-5) is used to calculate the receiver part-load efficiency – as a fraction of the receiver full power efficiency.

APPENDIX B
RESULTS OF EXTERNAL RECEIVER
THERMAL LOSS

The data used to evaluate the external receiver thermal loss were ten to thirty second data recorded over a thirty minute time interval for each test power level. Equation (A-17) from Appendix A was used to calculate the thermal loss. We used the methodology, which was described in the Evaluation Method section of this report, to select the actual value of a measured parameter for the thermal loss evaluation.

To determine the steady state values, actual values for each measured parameter, using eleven consecutive data tape time steps toward the end of each power level, were fit with straight lines using a least squares technique. We used the value from the data fit equation at the tenth time interval as the steady state value. Also, this same procedure for finding steady state values was done for the calculated receiver incident and absorbed powers. We used these data fit values to solve the equations in Appendix A. The equations in Appendix A are independent of the receiver incident power. The receiver incident power was used in Equation (1) to find the receiver efficiency to compare with efficiency results independent of incident power. Tables B-I, B-II, and B-III are summaries of the data used in the thermal loss evaluation and results from the thermal loss tests.

We used the average front surface temperatures from Equation (A-23) to calculate the predicted losses, Equation (A-28), listed in the Tables for the full power test level. These predicted losses were then used to calculate a "receiver efficiency using predicted loss" in the Tables, using Equation (A-19) in Appendix A. The "receiver efficiency using the measured loss" in the Tables also used Equation (A-19).

The uncertainty analysis for the random errors was done by incrementing each individual measured value on the data tape and finding the difference between the original thermal loss and that calculated with the incremented measured value. The uncertainty for each measured parameter, e.g. inlet temperature, outlet temperature, flow, etc., was assumed to be the standard deviation value from the average of that parameter for a given power level. The total random uncertainty was the root-sum-square of each individual measured value term uncertainty.

The uncertainty analysis for the bias errors was done by incrementing each measured parameter, e.g., all inlet temperatures or all outlet temperatures, and finding the difference between the original thermal loss and that calculated with the incremented measured parameter. The uncertainty for the measured parameter was assumed constant for each test power level, and the full power standard deviation value was used. The total bias uncertainty was the root-sum-square of

each individual parameter term uncertainty. Uncertainty analysis was done for both the measured loss, Equation (A-17), and the measured efficiency, Equation (A-19), for the full power test level.

To present the data from the thermal loss tests, we defined the following nomenclature to use as headings in the tables:

TIME   - solar time in hours (12.0 is solar noon)

INSOL   - measured direct normal insolation

INCPOW   - calculated receiver incident power

ABSPOW   - calculated receiver absorbed power

TIN   - measured receiver inlet water temperature

TOUT   - measured receiver outlet steam temperature

HEL   - number of heliostats tracking the receiver

TAMB   - ambient air temperature

WIND SP   - measured wind speed

WIND DIR   - measured wind direction

The data and results shown in Tables B-I, B-II, and B-III are for the three thermal loss tests we performed at Solar One. The first test, October 31, 1985, was before the receiver was repainted. The other two tests, March 19, 1986 and March 20, 1986, were both done after the receiver was repainted. Results from these thermal loss tests are discussed in the Receiver Thermal Loss section of this report.

TABLE B-I
DATA FROM THE RECEIVER THERMAL LOSS TEST
ON OCTOBER 31, 1985

Steady state test data

TIME	INSOL (w/m²)	INCPOW (MW$_t$)	ABSPOW (MW$_t$)	TIN (°C)	TOUT (°C)	HEL	TAMB (°C)	WIND SP (m/s)	WIND DIR (°)
11.64	850.1	18.68	11.32	156.04	425.80	890	19.8	5.56	264
11.97	882.9	39.32	28.24	186.36	442.89	1802	20.3	4.41	259
12.31	904.7	20.49	13.46	159.13	430.96	917	21.3	4.92	237

Thermal loss test results

Receiver predicted thermal loss	=	3.63 MW$_t$
Sum of the panel measured thermal losses	=	3.96 MW$_t$
Receiver measured thermal loss	=	4.36 MW$_t$
Measured thermal loss precision uncertainty	=	± 1.055 MW$_t$
Measured thermal loss bias uncertainty	=	± 0.728 MW$_t$
Receiver efficiency using incident power	=	71.8%
Receiver efficiency using predicted loss	=	77.8%
Receiver efficiency using measured loss	=	76.1%
Measured loss efficiency precision uncertainty	=	± 2.12%
Measured loss efficiency bias uncertainty	=	± 1.45%

TABLE B-II
DATA FROM THE RECEIVER THERMAL LOSS TEST
ON MARCH 19, 1986

Steady state test data

TIME	INSOL (w/m²)	INCPOW (MW$_t$)	ABSPOW (MW$_t$)	TIN (°C)	TOUT (°C)	HEL	TAMB (°C)	WIND SP (m/s)	WIND DIR (°)
11.48	979.2	22.00	16.10	162.22	421.37	880	17.1	3.90	131
11.97	982.7	45.23	36.96	188.97	440.29	1790	18.5	3.61	123
12.48	980.2	22.86	16.87	162.98	421.73	913	17.7	5.73	147

Thermal loss test results

Receiver predicted thermal loss	=	3.73 MW$_t$
Sum of the panel measured thermal losses	=	5.04 MW$_t$
Receiver measured thermal loss	=	4.91 MW$_t$
Measured thermal loss precision uncertainty	=	± 0.285 MW$_t$
Measured thermal loss bias uncertainty	=	± 0.390 MW$_t$
Receiver efficiency using incident power	=	81.7%
Receiver efficiency using predicted loss	=	85.1%
Receiver efficiency using measured loss	=	82.7%
Measured loss efficiency precision uncertainty	=	± 0.48%
Measured loss efficiency bias uncertainty	=	± 0.45%

TABLE B-III
DATA FROM THE RECEIVER THERMAL LOSS TEST
ON MARCH 20, 1986

Steady state test data

TIME	INSOL (w/m²)	INCPOW (MW$_t$)	ABSPOW (MW$_t$)	TIN (°C)	TOUT (°C)	HEL	TAMB (°C)	WIND SP (m/s)	WIND DIR (°)
11.51	980.5	21.96	15.97	161.25	436.16	880	21.3	4.43	97
12.01	983.8	45.30	36.70	199.73	434.00	1796	21.6	4.42	66
12.51	980.6	22.86	16.55	163.31	436.56	916	22.4	5.32	88

Thermal loss test results

Receiver predicted thermal loss	=	3.92 MW$_t$
Sum of the panel measured thermal losses	=	5.74 MW$_t$
Receiver measured thermal loss	=	5.56 MW$_t$
Measured thermal loss precision uncertainty	=	± 2.269 MW$_t$
Measured thermal loss bias uncertainty	=	± 0.537 MW$_t$
Receiver efficiency using incident power	=	81.0%
Receiver efficiency using predicted loss	=	84.7%
Receiver efficiency using measured loss	=	81.4%
Measured loss efficiency precision uncertainty	=	± 4.08%
Measured loss efficiency bias uncertainty	=	± 0.63%

REFERENCES

1. *10 MW$_e$ Solar Thermal Central Receiver Pilot Plant Receiver Cold Flow (Test 1010) and Receiver Steam Generation (Test 1030) Test Report,* McDonnell Douglas, MDC H0141, January 1983.

2. L. G. Radosevich, *Final Report on the Experimental Test and Evaluation Phase of the 10 MW$_e$ Solar Thermal Central Receiver Pilot Plant,* Sandia National Laboratories, SAND85-8015, 1985.

3. L. G. Radosevich, *Final Report on the Power Production Phase of the 10 MW$_e$ Solar Thermal Central Receiver Pilot Plant,* Sandia National Laboratories, SAND87-8022, 1988.

4. A. F. Baker and D. L. Atwood, *10 MW$_e$ Solar Thermal Central Receiver Pilot Plant Receiver Steam Generation (Test 1030) Evaluation Report,* Sandia National Laboratories, SAND83-8005, 1983.

5. A. F. Baker and D. L. Atwood, *Monograph Series No.2: 10 MW$_e$ Solar Thermal Central Receiver Pilot Plant and Receiver Performance Evaluation ,* Sandia National Laboratories, SAND85-8224, 1985.

6. *10 MW$_e$ Solar Thermal Central Receiver Pilot Plant Receiver Subsystem Analysis Report (RADL ITEM 4-1),* SAN/0499-27, MDC G8272, February 1980 (revised April 1982).

7. Pyromark is a product of TEMPIL Division, Big Three Industries, Inc., South Plainfield, NJ.

8. P. L. Leary and J. D. Hankins, *A User's Guide for MIRVAL – A Computer Code for Comparing Designs of Heliostat-Receiver Optics for Central Receiver Solar Power Plants,* Sandia National Laboratories, SAND77-8280, 1979.

9. A. H. Bowker and G. J. Lieberman, *Engineering Statistics,* Third Printing, Prentice-Hall, Inc., Englewood Cliffs, NJ., 1983.

10. *10 MW$_e$ Solar Thermal Central Receiver Pilot Plant Solar Facilities Design Integration Pilot Plant Station Manual (RADL ITEM 2-1), Volume 1, System Description,* SAN/0499-57, MDC G8544, September 1982 (Revised December 1985).

11. A. F. Baker, *Monograph Series No. 3: 10 MW$_e$ Solar Thermal Central Receiver Pilot Plant Solar Absorptance Measurements and Results,* Sandia National Laboratories, SAND86-8210, 1986.

102

12. R. F. Boehm, *Review of Thermal Loss Evaluations of Solar Central Receivers,* Sandia National Laboratories, SAND85-8019, 1985.

13. C. M. Randall, *Barstow Insolation and Meteorological Data Base,* The Aerospace Corporation, Report ATR-78(7695-05)-2, March 1978.

14. *Direct Normal Solar Radiation Data Manual,"* Solar Energy Research Institute, SERI/SP-281-1658, October 1982.

15. A. F. Baker, *Monograph Series, No. 4: 10 MW_e Solar Thermal Central Receiver Pilot Plant Heliostat Field Aimpoint Improvements,* Sandia National Laboratories, SAND85-8244, 1986.

16. D. L. Siebers, R. G. Schwind, and R. J. Moffat, *Experimental Mixed Convection Heat Transfer From a Large, Vertical Surface in a Horizontal Flow,* Sandia National Laboratories, SAND83-8225, July 1983.

17. D. L. Siebers and J. S. Kraabel, *Estimating Convective Energy Losses From Solar Central Receiver,* Sandia National Laboratories, SAND84-8717, April 1984.

18. F. Kreith, *Principles of Heat Transfer,* Third Edition, Intext Educational Publishers, New York and London, 1973.

19. J. C. Lippold, *Cracking of Alloy 800 Tubing in Superheated Steam sections of the Solar One Central Receiver,* Sandia National Laboratories, SAND85-8602, July 1985.

U.S. Department of Energy (4)
Forrestal Building
Code CE-314
1000 Independence Avenue, S.W.
Washington, D.C. 20585
Attn: H. Coleman
      S. Gronich
      F. Morse
      M. Scheve

U.S. Department of Energy
Forrestal Building, Room 5H021C
Code CE-33
1000 Independence Avenue, S.W.
Washington, D.C. 20585
Attn: C. Carwile

U.S. Department of Energy
Albuquerque Operations Office
P.O. Box 5400
Albuquerque, NM 87115
Attn: D. Graves

U.S. Department of Energy
San Francisco Operations Office
1333 Broadway
Oakland, CA 94612
Attn: R. Hughey

University of California
Environmental Science and Engineering
Los Angeles, CA 90024
Attn: R. G. Lindberg

University of Houston (2)
Solar Energy Laboratory
4800 Calhoun
Houston, TX 77704
Attn: A. F. Hildebrandt
      L. Vant-Hull

University of Kentucky
Dept. of Chemical Engineering
Lexington, KY 40506
Attn: J. E. Funk

University of Utah
Mechanical & Ind. Engineering Dept.
Salt Lake City, Utah 84112
Attn: R. F. Boehm

Analysis Review and Critique
6503 81st Street
Cabin John, MD 20818
Attn: Carlo La Porta

Babcock and Wilcox
91 Stirling Avenue
Barberton, OH 44203
Attn: D. Young

Bechtel Group, Inc. (2)
P.O. Box 3965
San Francisco, CA 94119
Attn: P. DeLaquil
        S. Fleming

Black & Veatch Consulting Engineers (2)
P.O. Box 8405
Kansas City, MO 64114
Attn: J. C. Grosskreutz
        J. E. Harder

California Energy Commission
1516 Ninth St., M/S 40
Sacramento, CA 95814
Attn: A. Jenkins

California Public Utilities Com.
Resource Branch, Room 5198
455 Golden Gate Ave.
San Francisco, CA 94102
Attn: T. Thompson

Centro Investigations Energetica
Medroansental Technologie (CIEMAT)
Avda. Complutense, 22
28040 Madrid
Spain
Attn: F. Sanchez

DFVLR RF-ET
Linder Hohe
D - 5000 Koln 90
West Germany
Attn: Dr. Manfred Becker

Electric Power Research Institute (2)
P.O. Box 10412
Palo Alto, CA 94303
Attn: J. Bigger
E. DeMeo

Foster Wheeler Solar Development Corp.
12 Peach Tree Hill Road
Livingston, NJ 07039
Attn: S. F. Wu

Georgia Institute of Technology
GTRI/EMSL Solar Site
Atlanta, GA 30332

D. Gorman
5031 W. Red Rock Drive
Larkspur, CO 80118

Jet Propulsion Laboratory
4800 Oak Grove Drive
Pasadena, CA 91103
Attn: M. Alper

Los Angeles Department of Water and Power
Alternate Energy Systems
Room 661A
111 North Hope St.
Los Angeles, CA 90012
Attn: Hung Ben Chu

Martin Marietta Aerospace
P.O. Box 179, MS L0450
Denver, CO 80201
Attn: H. Wroton

McDonnell Douglas (4)
MS 49-2
5301 Bolsa Avenue
Huntington Beach, CA 92647
Attn: D. Barron
R. L. Gervais
J. E. Raetz
S. Saloff

Meridian Corporation
5113 Leesburg Pike
Falls Church, VA 22041
Attn: D. Kumar

Public Service Company of New Mexico (2)
M/S 0160
Alvarado Square
Albuquerque, NM 87158
Attn: T. Ussery
A. Martinez

Olin Chemicals Group
120 Long Ridge Road
Stamford, CT 06904
Attn: J. Floyd

Pacific Gas and Electric Company
77 Beale Street
San Francisco, CA 94106
Attn: J. Laszlo

Pacific Gas and Electric Company (4)
3400 Crow Canyon Road
San Ramon, CA 94526
Attn: G. Braun
T. Hillesland, Jr.
B. Norris
C. Weinberg

Rockwell International
Rocketdyne Division
6633 Canoga Avenue
Canoga Park, CA 91304
Attn: J. Friefeld

Sandia Solar One Office
P.O. Box 366
Daggett, CA 92327
Attn: A. Snedeker

Science Applications International Corp.
10401 Roselle Street
San Diego, CA 92121
Attn: B. Butler

Solar Energy Research Institute (2)
1617 Cole Boulevard
Golden, CO 80401
Attn: B. Gupta
D. Hawkins

Solar Kinetics Inc.
P.O. Box 47045
Dallas, TX 75247
Attn: J. A. Hutchison

Southern California Edison
P.O. Box 325
Daggett, CA 92327
Attn: C. Lopez

Stearns Catalytic Corp.
P.O. Box 5888
Denver, CO 80217
Attn: T. E. Olson

Stone and Webster Engineering Corporation
P.O. Box 1214
Boston, MA 02107
Attn: R. W. Kuhr

6000	D. L. Hartley; Attn: V. L. Dugan, 6200
6220	D. G. Schueler
6222	K. R. Boldt
6222	W. A. Couch
6222	C. Maxwell
6222	J. V. Otts
6226	J. T. Holmes (10)
6226	C. E. Tyner
8000	J. C. Crawford; Attn: R. J. Detry, 8200
	P. L. Mattern, 8300
	R. C. Wayne, 8400
	P. E. Brewer, 8500
8100	E. E. Ives; Attn: J. B. Wright, 8150
	D. J. Bohrer, 8160
	R. A. Baroody, 8180
8130	L. A. Hiles
8133	A. F. Baker (20)
8133	L. G. Radosevich
8133	A. C. Skinrood (3)
8133	D. N. Tanner
8244	C. Hartwig
8535	Publications Division for OSTI (10)
8535	Publications/Technical Library Processes, 3141
3141	Technical Library Processes Division, (3)
8524-2	Central Technical Files (3)